Oxide glasses under pressure: Recent insights from experiments and simulations

Du, Tao; Sørensen, Søren Strandskov; To, Theany; Smedskjær, Morten Mattrup

Published in:
Journal of Applied Physics

DOI (link to publication from Publisher):
10.1063/5.0088606

Publication date:
2022

Document Version
Accepted author manuscript, peer reviewed version

Oxide Glasses under Pressure: Recent Insights from Experiments and Simulations

Tao Du[†], Søren S. Sørensen[†], Theany To[†], Morten M. Smedskjaer[*]

Department of Chemistry and Bioscience, Aalborg University, Aalborg, Denmark

[†] These authors contributed equally

* Corresponding author. e-mail: mos@bio.aau.dk

Abstract:

Deciphering the structure-property relations of densified oxide glasses is a problem of longstanding interest. For example, it is important for understanding the fracture mechanism under sharp contact loading as well as fabricating glasses with tunable physical characteristics. Recent advances in both experimental and simulation techniques have prompted research breakthroughs in understanding the response of glasses to high pressure. In this Perspective, we first briefly discuss the facilities for the high-pressure treatment of glasses, including *in situ* and *ex situ* investigations. The recent work on pressure-induced structural changes of archetypical oxide glass families (silicates, germanates, borates, aluminates, phosphates) is then be discussed and related to the changes in macroscopic properties induced by densification, as densification treatment can be used to produce oxide glasses with improved hardness, stiffness and toughness. We also discuss the new insights from atomistic simulations combined with topological analysis tools to unravel the densification mechanism of oxide glasses on the medium-range order length scale. Drawing on these recent studies, we clarify how densification treatment has proved to be an important tool to both understand the disordered nature of glasses and tune their physical properties, although many open questions and challenges remain that require further investigations.

1. Introduction

Oxide glasses constitute around 95% of the produced commodity and specialty glass products worldwide as they find applications in various important sectors from architecture and information technology to energy and healthcare [1]. As a vital component of the modern world, it is therefore important to understand their fundamental behavior, especially their structure-property relations. The cations in oxide glasses are traditionally classified as network formers, modifiers, or intermediates. While network-forming cations (e.g., silicon, phosphorous, and boron) form the glass network backbone by making strong, directional (covalent) bonds with oxygen, the network-modifying cations (e.g., alkali and alkaline earth) form weaker, non-directional (ionic) bonds with oxygen. The role of network intermediates, as either a network former or modifier, depends on the chemical environment. The properties of glasses, from chemical to thermal and mechanical, depend on the network structure. This includes how it responds to changes in glass composition, but also changes in state variables such as temperature and pressure.

Changes in structure and properties can be gradual or abrupt as in the case of polyamorphic transitions when pressure is varied [2-4]. Such transitions are, e.g., present in amorphous water as well as other glass-forming systems under both varying temperature and pressure conditions [5,6]. Indeed, the structure and properties of oxide glasses can be significantly influenced under high pressures and such pressures are important for the following scenarios. First, for the fracture mechanics response of glasses, sharp-contact loading leads to stresses in the range of GPa. Such loading is an important failure mechanism in the field for, e.g., cover glasses for electronic devices, and can be mimicked in the laboratory via normal (typically Vickers) or lateral (scratch) indentation [7,8]. Designing glass structures with the ability to adapt their local structure to the high stress can be used to improve their damage resistance [9]. Second, high pressures can be used to either momentarily or permanently densify glasses (that is, elastic or plastic deformation, respectively) and thus tune their physical properties in a reversible or irreversible fashion. The extent of densification is controlled by the choice of pressure, temperature, and time of treatment, yet it is also highly dependent on the glass composition. If the glass is subjected to high pressure at a temperature when the treatment time is above the structural relaxation time and subsequently frozen-in under pressure, the glass can be regarded as permanently densified

[10]. This assumes that its glass transition temperature (T_g) is significantly above the ambient temperature. Third, the response of silicate glass-forming liquids to pressure (and temperature) is of great importance for geosciences, including understanding the evolution of Earth into its current stratified structure from magma oceans in the early Earth history as well as melting, migration, and emplacement of melts in the Earth's surfaces and interiors [11].

In this Perspective, we will discuss the recent advances in understanding the response of oxide glasses and glass-forming liquids to high pressure, especially as it relates to their structure-property evolution (Fig. 1). First, we briefly discuss the typical facilities used to induce and characterize high-pressure treatment of glasses, including both cold and hot compression as well as *in situ* and *ex situ* investigations. Then we will present the recent breakthrough in understanding pressure-induced structural changes across different length scales (short-range and medium-range order) and in different oxide glass families (silicates, germanates, borates, aluminates, phosphates). This will be followed by discussing the property changes that can be induced in permanently densified glasses recovered from the high-pressure state, including the perspectives for using hot compression as a post-treatment method. The recent insights gained from emerging characterization of densification based on atomistic simulation studies will also be covered. We conclude with an outlook on open questions and challenges within the field of high-pressure glass science. We refer the reader to existing papers [10,12-14] for more complete (historic) reviews on the impact of pressure on glass structure and properties.

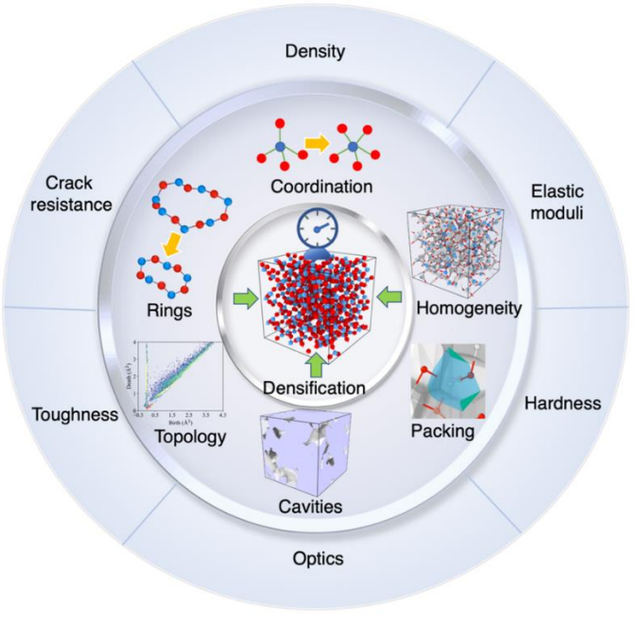

Figure 1. Densification of oxide glasses affects the disordered structure at different length scales and in turn a variety of macroscopic properties.

2. High Pressure Facilities

2.1. Cold vs. hot compression

The densification behavior of oxide glasses strongly depends on the temperature at which the pressure is applied [10]. Pressure treatments are therefore commonly referred to as either cold or hot compression, where the former is performed at room temperature or at a temperature significantly below T_g, while the latter is performed at high temperature around or above T_g.

The facilities used for cold compression include uniaxial compression, diamond anvil cells (DACs), multianvil devices, and indentation methods. Since pressure is equal to the applied load divided by the applied area, the pressure may easily be increased by reducing the applied area. Uniaxial compression systems consist of two dies made of hard materials such as tungsten carbide cobalt (WC-Co), which are flat at the surface next to the sample and enlarge with a conical angle 170 ° toward the upper and lower supports [2]. The sample in-between the two dies is in the form of a thin disk with a diameter of 5 to 8 mm and a thickness of 0.15 to 0.25 mm [2]. The sample can be compressed up to a pressure of around 14 GPa using this setup. High loading rates

(> 0.2 GPa s^{-1}) give rise to larger densification effects of the glass compared to a lower loading rate (< 0.05 GPa s^{-1}). For example, the cold compression at 13.5 GPa of $10Na_2O$-$90SiO_2$ glass (in mol%) results in a relative density increase of 11% in the case of high loading rate, while the increase is only 6% in the case of using a low loading rate [2]. A DAC consists of two opposing diamonds with a glass sample compressed between the tips. The applied pressure, which is measured by means of the *in situ* ruby-fluorescence method, can remain hydrostatic up to 12 GPa and quasi-hydrostatic above [15].

The multianvil device consists of multiple anvils made of hard and strong materials such as WC-Co, sintered polycrystalline diamond, or boron nitride and a cell to keep the anvils together. The anvils are designed to have a large surface area on the support side and a relatively small surface area on the applied pressure side. Various multianvil devices exist, including pyrophyllite tetrahedron, trigonal-bipyramidal, cubic (also known as DIA diamond shape), octahedral, and three-stage spherical anvil devices. For oxide glasses, an octahedral anvil is often applied, and it can pressurize the sample up to 25 GPa. Figure 2 shows the plan view of an octahedral anvil device. More details about all the multianvil devices with their history can be found in Ref. [16]. Indentation including Vickers micro-indentation and nano-indentation testing results in glass densification upon applying a sharp contact loading on the glass surface in the form of hydrostatic stresses, which are in the same magnitude (~5-10 GPa) as using the multianvil devices. Upon indentation, both volume conservation shear flow as well as densification occur and can be estimated. A well-known oxide glass, silica glass, deforms predominantly through densification, unlike the case of bulk metallic or metal-organic framework glasses, where volume conservative shear flow dominates [17,18].

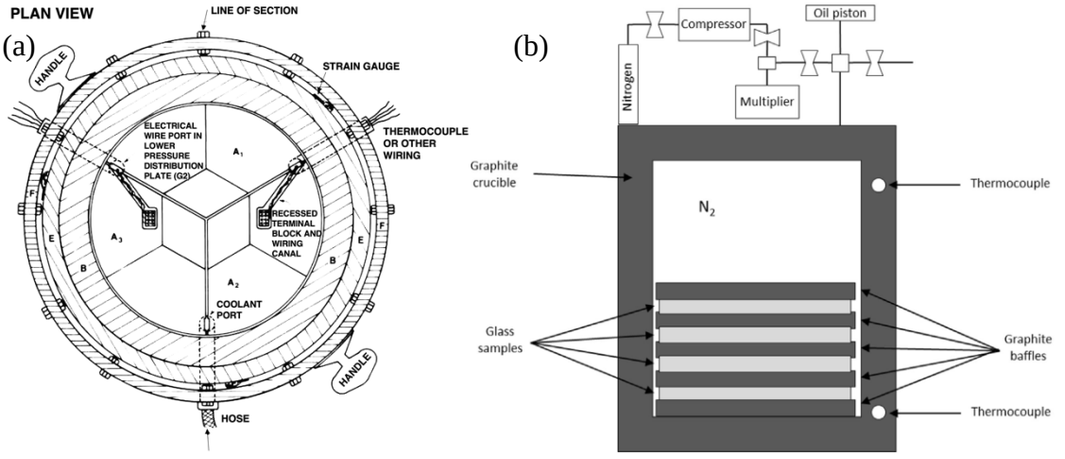

Figure 2. Typical compression facilities. (a) Schematic plan view of multianvil module for cold compression [19]. (b) Schematic illustration of the gas pressure vessel method for hot compression [10]. (a) is adapted with permission from Walker *et al.*, *Am. Mineral.* **1990**, *75* (9-10), 1020-1028. Copyright 1990 American Mineralogist. (b) is reproduced from Kapoor *et al.*, *Front. Mater.* **2017**, *4*, 1. under open access license.

For hot compression, the facilities described for cold compression can also be used, with the maximum temperature depending, e.g., on the anvil and indenter materials. Since compression begins to influence oxide glasses at much lower pressure at higher temperature, other methods not limited to small compression areas can also be applied. For example, hot compression facilities in the form of isostatic compression by gas chamber vessels [10]. Here, nitrogen gas is usually used as the compression medium due to its low permeability in oxide glasses compared to, e.g., helium [20]. For example, densification of bulk samples of dimension above 10 mm has been demonstrated at a maximum pressure of 2 GPa [21].

An advantage of cold compression is the ease of performing *in situ* investigations (see Section 2.2), but due to the long relaxation times, cold compression often results in a metastable densification [3]. On the other hand, hot compression can lead to permanent densification (i.e, densification that is stable over time at room temperature) when the glass is given sufficient time to equilibrate to the high-pressure/high-temperature environment. Figure 3 shows the increase in density of magnesium silicate and sodium borosilicate glasses with temperature, highlighting three distinct regions [10]. The elastic region is region (1), in which the compression temperature, at pressure below or equal to 2 GPa, is relatively low compared to T_g. It is

noteworthy how higher induced pressure lowers the temperature requirement for significant density changes in region (1). Region (2) is where the degree of densification increases with increasing temperature, which is also the case for region (3) but with a smaller increase in density with temperature. In both regions (2) and (3), the densification is inelastic upon decompression.

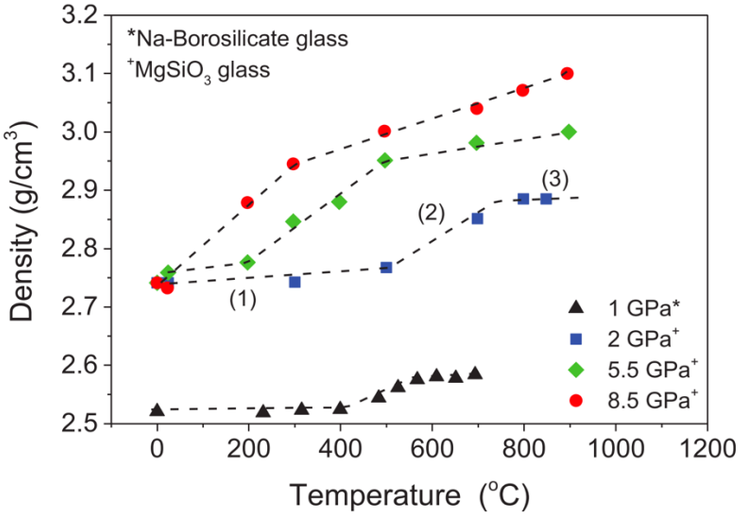

Figure 3. Density of magnesium silicate (T_g = 766 °C) and sodium borosilicate (T_g = 567 °C) glasses as a function of compression temperature [10]. The black symbols represent the magnesium silicate glasses, while the colored symbols represent the sodium borosilicate glasses. Reproduced with permission from Kapoor *et al.*, *Front. Mater.* **2017**, *4*, 1. under open access license.

2.2. In situ investigations

Both cold and hot compression can be used for *in situ* and *ex situ* investigations of compressed glasses. *In situ* investigation refers to measurements performed while pressure is being applied, whereas *ex situ* refers to measurements after the glass is decompressed to ambient conditions. However, both investigations are made on the glass that is compressed, i.e., the glass is in a different state relative to its as-prepared counterpart. For the *ex situ* experiment, various investigations of both structure and properties of the compressed glasses can be performed as described in Sections 3-4. In the following, we focus on *in situ* investigations.

Most *in situ* investigations of compressed glasses have focused on pressure-induced changes in the glass structure by means of Raman, nuclear magnetic resonance (NMR) and X-ray diffraction techniques [22-27]. Such *in situ* high-pressure techniques require a cell that can induce high pressure and consist of windows that are transparent to the radiation of interest. The most popular cell is the DAC, for which the windows are usually also made of diamond. Diamond is a well-suited material for vibrational spectroscopy because it provides low-fluorescence, especially for hot compression facilities [23]. However, diamond has relatively narrow Raman bands that limits the fraction of the spectral range. As such, the use of moissanite or sapphire anvils can allow access to the full Raman/infrared spectral range [24]. For example, Benmore et al. [25] used a DAC with perforated diamond and x-ray diffraction to study the structure of silica glass up to a pressure of ~45 GPa. A few pieces of ruby was packed with the silica glass and used to determine the applied pressure based on the ruby flurorescence technique. Morard et al. [26] also used a DAC in their *in situ* x-ray diffraction study on three silicate glasses using both static and dynamic (by laser shock) compression. For the static compression, pressures above 100 GPa can be reached. Khanna et al. [27] also used a DAC in their *in situ* high-pressure neutron diffraction and Raman spectroscopy study of barium tellurium oxide glasses. For the Raman spectroscopy measurements, they immersed the glass sample in the mixture of methanol and ethanol as the pressure-transmitting medium for the complete hydrostatic compression. For the neutron diffraction measurements, no pressure transmitting medium was used to avoid background scattering peaks from the transmitting material. It is noteworthy that the transmitting media in DAC can possibly induce a shear component, leading to a departure from a purely hydrostatic pressure and hence explaining the differences between experiments. A summary of different transmitting media in DAC can be found in Ref. [15]. For example, a usage of 20:4:1 methanol-ethanol-water as a transmitting media can only keep the pressure to be purely hydrostatic up to a value of 12 GPa. Any pressure above this threshold will induce shear stresses during compression-decompression cycles, leading to non-purely hydrostatic pressure, called quasi-hydrostatic [15,28].

Beside multianvil devices, structural studies have also been done *in situ* under indentation. For example, Gerbig and Michaels [29] used *in situ* Raman spectroscopy to measure the deformation region of the indented glasses. Figure 4 shows the schematic of the indentation device used for Raman microscopy. From

the inverted optical microscope, the conventional bright field reflected white light imaging is used to switch to a laser port for the beam entry in the light path of Raman spectroscopy (see Ref. [30] for details). To perform the *in situ* Raman measurement, the indenter is held at the desired indentation load and the confocal laser spot focus is moved from the sample surface down into the glass matrix.

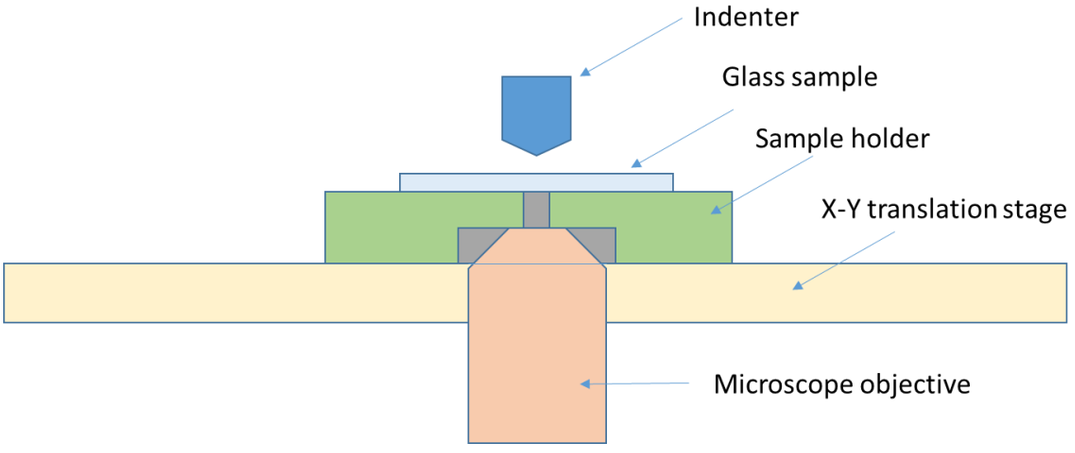

Figure 4. Schematic of the main components of instrumented indentation device for coupling with Raman microscopy.

3. Glass Structure

While high-pressure facilities are the means, the enlightenment of glass structure and properties is the goal of many high-pressure studies. For the glass structure, many questions remain unanswered. This is due to the large number of new and complex glass compositions as well as processing methods, exploiting the fact that glass structure, unlike that of crystals, is highly dependent on both thermal and pressure history. It is also due to the lack of an analytical framework based on symmetries and invariances commonly used for structure solving in crystals, as such symmetries are inherently absent in amorphous materials. In this section, we will explore the recent advances in understanding of the structure of densified oxide glasses. From our literature review, several trends are clear. First, the interest in new and unconventional glass compositions for optimizing, e.g., mechanical properties has sparked an inherent interest in their structure. Second, new experimental characterization techniques have emerged, commonly allowing *in situ* measurements at pressures surpassing 100 GPa (so-called megabar pressures). Lastly, improved computational power at high-performance

computing facilities allow for studying larger systems at higher levels of complexity, e.g., by using reactive potentials or *ab initio* simulations. However, despite an increased level of understanding in the past decade, even the most compositionally simple model glasses continue to provide new and surprising insights.

3.1 Silicates

The most studied oxide glass system is the archetypical silica (SiO_2) glass, but despite its compositional simplicity, it holds several structural peculiarities and anomalies. For example, the pressure dependence of the Si coordination environment has been intensively discussed, owing to new possibilities of exploring pressure regimes above 100 GPa. Previously, by increasing the hydrostatic pressure to around 100 GPa at room temperature (i.e., cold compression), a gradual change of the coordination number of silicon (CN_{Si}) with pressure was observed in distinct pressure regions [25,31,32]. Specifically, in the region of 0-20 GPa, CN_{Si} remains at a value of 4, but then CN_{Si} gradually increases towards 5 in the region of 20-40 GPa before increasing further and plateauing around $CN_{Si} \approx 6$ at 40-90 GPa. Based on NMR studies, this transition of CN_{Si} from 4 to 6 has been found to go through a stable species of 5-coordinated Si and to be highly dependent on fictive temperature, at least in modified silicates [33,34]. On the other hand, atomistic simulation results have confirmed that the densification of SiO_2 structure is correlated with a structural transition to high-coordinated phases (e.g., SiO_5- or SiO_6-phases) and further suggest the importance of considering edge- as well as face-sharing between polyhedra [35]. Figure 5 presents the pressure dependence of CN_{Si} of glassy SiO_2 as measured by several groups [36-38], including recent studies at pressures above 90 GPa based on various types of X-ray scattering. Notably, increasing the pressure above ~90 GPa in cold compression has provided the first experimental evidence of CN_{Si} above six.

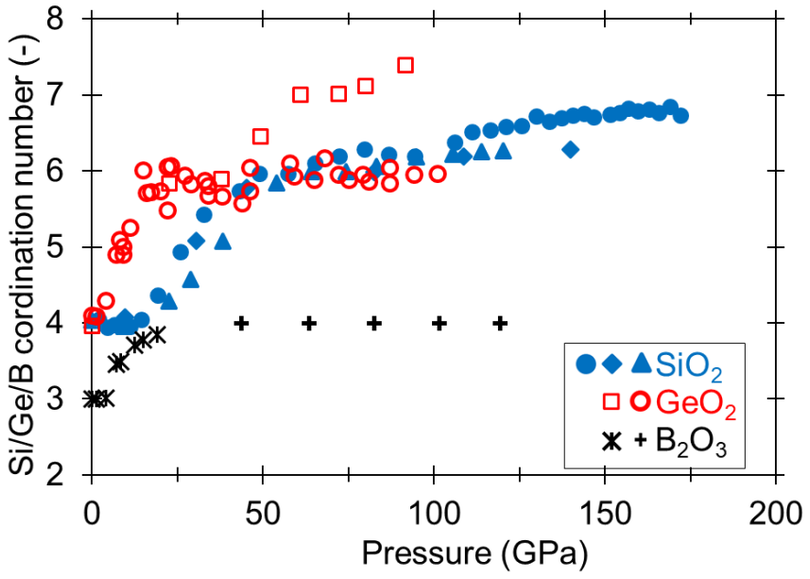

Figure 5. Pressure dependence of first shell coordination number of Si, Ge, and B in SiO_2 [36-38], GeO_2 [39,40], and B_2O_3 [41,42] glasses, respectively, in cold compression setups up to megabar pressures. Colors indicate glass former.

Information of coordination numbers at high pressures is crucial for understanding not only the coupling between glass structure and properties, but also of high interest for understanding the processes in the Earth mantle, where pressures above 100 GPa can be reached. An example of this interest is recent cold compression measurements of glassy $MgSiO_3$ up to ~110 GPa [26]. Although restricted by a low *Q*-range and hence the inability to study real space correlations, the first sharp diffraction peak (the peak of the lowest momentum transfer, i.e.,*Q*,-value in the structure factor) as well as the principal peak (the peak of the second-lowest *Q*-value in the structure factor) of glassy $MgSiO_3$ was found to feature a similar densification route as that of pure SiO_2 under both compression in diamond anvil cells as well as in shock compression experiments [26,36].

In relation to the changes of coordination numbers in pure SiO_2, the average Si-O bond length at pressures below 10 GPa is ~1.62 Å, and then linearly increases to ~1.69 Å for pressure values up to 40 GPa, and finally exhibits a linear decrease to ~1.65 Å at 170 GPa for a number of cold compression experiments [25,32,36,43]. Based on *ab initio* molecular dynamics (MD) simulations of permanently densified SiO_2

glasses, the Si-O bond becomes less covalent-like and the O-Si-O bond angle distribution becomes broader upon densification [44]. As the Si-O-Si bond angle distribution describes the local structure around O atoms, it suggests the existence of three-coordinated oxygens (so-called triclusters) from 31 GPa, the coexistence of both triclusters and four-coordinated oxygens (so-called quadclusters) at 140 GPa, and finally the prevalency of quadclusters at 200 GPa [37]. We note how X-ray Raman scattering measurements, also performed as cold compression, support these findings [45].

The role of oxygen in relation to compression of SiO_2 (and other glass network formers such as Ge and B) is also evident from the important role of the oxygen packing fraction (η_O) [47], which is a measure of how much space oxygen atoms occupy in the network glass structure (i.e., η_O varies between 0 and 1). The calculation of η_O builds on the idea that it is not only the anion/cation radii ratio that controls the overall structure [46] and η_O has been proposed as an intuitive probe for rationalizing the cation coordination number changes in compressed SiO_2, GeO_2, and B_2O_3 glasses. As shown in Fig. 6a, for SiO_2, the higher coordinated polyhedra ($CN > 4$) start to form from SiO_4 tetrahedra when η_O>0.58, while most of the Si tetrahedra has transformed into SiO_6 octahedra when η_O reaches η_O~0.60 [47]. More recently, a modified η_O calculation method was suggested [36], which also shows a positive correlation between η_O and *CN* for SiO_2 and GeO_2 glasses, yet finding that the η_O eventually decreases at high pressures and provides a non-intuitive relation with coordination number (Fig. 6b). This correlation between topological ordering and η_O in the structure of oxide glasses under high pressure has been further examined based on Bader's atoms-in-molecules (AIM) theory [48]. Building on the structures generated from *ab initio* MD simulations, the atomic volume ratios of O/Si and O/Ge calculated from AIM theory do not keep constant with pressure, which has been attributed to how the electronic structure changes under pressure. Therefore, the scaling rule of bond lengths to atomic sizes should be changed with pressure. Thus, although η_O is indeed structurally intuitive, it relies on a simplified estimation of the radius of O atoms and may thus be a too simple metric for explaining *CN* changes at extreme pressures [48,49].

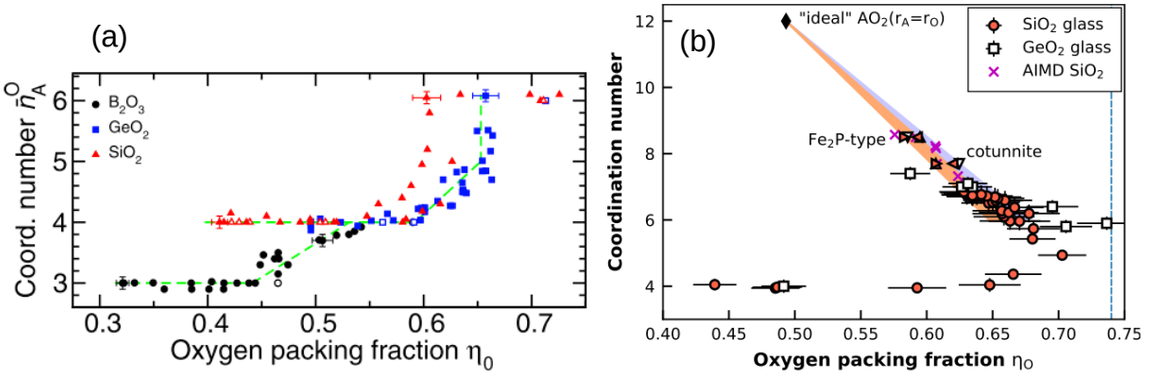

Figure 6. (a) Cation coordination number dependence on oxygen packing fraction (η_O) in SiO_2, GeO_2, and B_2O_3 glasses based on the method of Zeidler *et al*. [47]. Adapted with permission from Zeidler *et al*., Proc. Natl. Aca. Sci. U.S.A. **111**, 10045 (2014) under open access license. (b) Cation coordination number dependence on η_O for SiO_2 and GeO_2 glasses based on the method of Prescher *et al*. [36]. Reproduced with permission from Prescher *et al*., Proc. Natl. Aca. Sci. U.S.A. **114**, 10041 (2017) under open access license.

Another approach for quantifying both short-range order (SRO) and medium-range order (MRO) structural changes is through NMR spectroscopy, since silicon has the naturally abundant half-spin NMR-active ^{29}Si isotope, making NMR measurements feasible without enrichment [50]. Indeed, NMR remains to be the method of choice to directly probe the coordination number and Q^n speciation of silicon in glasses and for accessing more advanced correlations between different types of coordinated species (so-called 2D and 3D experiments), ultimately deducing MRO structural information. For example, in a recent study, ^{7}Li, ^{17}O and ^{29}Si magic angle spinning NMR measurements were performed on pre-compressed modified Na-Li silicates in the $(1\text{-}x)Na_2O\text{-}xLi_2O\text{-}3SiO_2$ series with $x \in \{0.25, 0.5, 0.75\}$ [51]. The study showed a pressure-induced increase in the coordination numbers of Li, Si, and O, yet also a significant pressure dependence of the non-bridging oxygen content (and hence the overall network polymerization) upon changing the Li-to-Na ratio, with Li-rich glasses featuring a higher degree of polymerization. This highlights the important contribution of the network modifiers on the overall pressure response [51]. We note how *in situ* NMR studies are often limited to rather low pressures compared to, e.g., diffraction experiments due to the complexity of preparing *in situ* high-pressure NMR cells [22].

3.2 Germanates

Since Ge and Si are in the IVA group of the periodic table, GeO_2 is considered as a chemical and structural analogue of SiO_2, i.e., the GeO_2 structure is based on corner-sharing (by one common oxygen) units of [GeO_4] tetrahedra. While germanate glasses are of smaller industrial interest due to the much higher raw material cost, they find specialized applications, e.g., within optics [52]. Fundamental understanding of their structure-property relations is particularly interesting due to their non-monotonic (anomalous) change in Ge CN upon modifier addition [53]. In fact, it was measurements on glassy GeO_2 [40] that helped spark the major interest in the coordination state of various glass formers at megabar (>100 GPa) pressures. Namely, X-ray diffraction measurements of GeO_2 in a cold compression setup showed how Ge increases its coordination number from 4 to 6 in the pressure range of 0-20 GPa (again, possibly with a five-fold transition state [48,54]), before the Ge *CN* increases further to an average coordination number of ~7 at around 90 GPa [40]. However, we note that these findings have later been questioned by X-ray emission spectroscopy measurements, finding the Ge coordination number to remain stable after reaching the value of 6 at a pressure of ~100 GPa [39]. It has been noted that the latter diffraction measurements could be faulty due to wrong estimations of sample densities at high pressures. Later, it has been argued that distortion of Ge polyhedra upon increasing pressure is the dominant densification mechanism after reaching CN_{Ge}=6.

A compilation of recent CN_{Ge} data from diffraction studies on GeO_2 glass is presented in Figure 5. It is also interesting to note that three density vs. pressure regimes exist for glassy GeO_2 (0-20 GPa; 20-80 GPa; >80 GPa) under cold compression [55], although these provide no direct answers regarding the coordination state. By means of MD simulations, it has been reported that upon compression, the structure of GeO_2 gradually transitions from tetrahedral to octahedra network as edge-sharing (by two common oxygens) is replaced by face-sharing (by three common oxygens). Since the Ge-Ge pair distance in corner-sharing units is much larger than that in edge-sharing and face-sharing units, there will be a split in the first peak of the Ge-Ge pair distribution function with an increase in pressure [56]. Meanwhile, the bond angles also exhibit some transitions upon densification [57]. At ambient pressure, the Ge-O bond length is approximately 1.74 Å, and the Ge-O-Ge bond angle is centered at around 125° with a small peak at around 85° [58]. When pressure

increases from 0 to 20 GPa, the O-Ge-O bond angle is mainly centered at 90° with a minor peak at 170°. The 85° and 90° peaks in the Ge-O-Ge bond angle distribution are ascribed to the edge-shared tetrahedra and octahedra, respectively [57]. The corner- and edge-sharing bonds are dominant in densified GeO_2 glass and found throughout the structure, while the face-sharing bonds are not uniformly distributed, leading to a heterogeneous structure [58]. The dynamical properties of GeO_2 glass will change accordingly upon densification due to the transition from GeO_4- to GeO_6- polyhedra. The low and high frequency bands of the vibrational density of states correspond to the vibration of inter- and intrapolyhedra, respectively. Notably, with an increase in density, the low frequency band of vibrational density of states becomes a clear peak while the high frequency band becomes broader and flatter [59]. Furthermore, we note that the literature on MRO structure and its pressure dependence in GeO_2 glasses is generally very sparse, but a recent study has shown that applying pressures of ~3 GPa combined with high temperatures activates the structural reorganization [60].

Apart from the *CN* data on pure GeO_2 glass, these measurements have later been complemented by X-ray absorption spectroscopy measurements of a more complex $NaAlGe_3O_8$ glass up to ~130 GPa of cold compression [61], showing qualitatively similar behavior to GeO_2, i.e., a transition from a tetrahedral to an octahedral coordination state with increasing pressure. Furthermore, the Na and Al atoms significantly altered the glass properties by providing a higher network compressibility. This was ascribed to the reduced rigidity, especially provided by the voids surrounding Na ions, eventually causing the complete transition of Ge to an octahedral state at higher pressures (~30 GPa for $NaAlGe_3O_8$ compared to 20 GPa for GeO_2). This was observed despite the presence of polyhedra with *CN*>4 in the as-made $NaAlGe_3O_8$ glass as caused by the germanate anomaly [39,61].

3.3 Borates

The boron coordination state in B_2O_3 glass has also attracted widespread attention [41,62-65]. Several studies have investigated the pressure-induced changes in SRO in the range of ~0-20 GPa [41,62], reporting that the boron coordination gradually increases with increasing pressure from 3 at 0 GPa to ~4 at ~23 GPa. Recent work has also shown evidence of four-fold coordinated boron being the sole component in glassy B_2O_3 up to

at least ~120 GPa of pressure in cold compression [42]. We have included the data from Refs. [41,42] for B_2O_3 to the plot in Figure 5. Interestingly, several authors have attempted to clarify which species emerge beyond the tetrahedral coordination state at higher pressures. In the crystalline state, *ab initio* simulations have predicted a coordination transition directly from 4 to 6, skipping the five-fold coordinated state, ultimately creating new superhard materials [66]. This stands in contrast to previous simulations of glassy B_2O_3, predicting the presence of both five- and six-fold coordinated boron at pressures above ~150 GPa [62,63]. Given the recent advances in high-pressure studies, experimental confirmation (or contradiction) of these predictions is expected to emerge in the future.

Like silicon, boron has the advantage of having a highly NMR active isotope (^{11}B), allowing for simple quantification of different coordination numbers, but also for specifically targeting correlations at longer length scales than those of the first coordination shell. As an example, double quantum magic angle spinning ^{11}B NMR was used to study Na_2O-$8B_2O_3$ glasses hot-compressed in a multi-anvil setup up to 9.2 GPa [67]. This study showed evidence of prevalence for glassy inhomogeneity. Specifically, similar boron-coordination environments (B^{III} and B^{IV}) were found to cluster, but such clustering was found to decrease upon increasing pressure. This type of inhomogeneity is interesting, given that inhomogeneity on the MRO length scale has been reported to diminish at higher pressures for SiO_2 [68,69]. We expect the pressure-induced change in MRO structure of borate glasses to be addressed further in future work, especially considering their accessibility by NMR measurements.

3.4 Mixed network formers

Glasses with a single network former are great model systems due to their compositional simplicity, but the mixing of network formers provides additional degrees of freedom to alter the structure and properties of glasses. Indeed, this is used in most industrial glasses, e.g., modified aluminosilicate glasses as substrate and cover glasses in personal electronic devices. There is also an interest in understanding the pressure response of such systems related to the inner mantle constituents. For example, two complex mixed modifier (Na, Sr, Mg) aluminogermanosilicate glasses were found to feature a qualitatively similar evolution of the Ge coordination number with increasing pressure (up to 164 GPa under cold compression) as that for pure GeO_2

[70]. A significantly larger compressibility of the Ge-O bond in the mixed glass system compared to that in pure GeO_2 was explained by the tendency of the latter to densify through distortion rather than compression. The authors ascribed this effect to the presence of the modifying ions, thus highlighting the importance of also studying glasses with network modifiers. Such importance of the network modifier has also previously been noted in aluminoborosilicate glasses (*E*-glasses) where the observed densification upon isostatic hot compression at ~0.5 GPa can only partially be explained by the change of coordination numbers of network formers [71]. Other studies have probed the silicon and aluminium speciation in permanently densified (up to 24 GPa) magnesium aluminosilicate glasses using *ex situ* NMR spectroscopy [72]. While the Si coordination remained unchanged after decompression in the studied pressure interval, that of Al experienced permanent changes after decompression for a pressure of only 5 GPa at room temperature. At higher pressures, a transition region of increasing *CN* between 5-15 GPa was observed, before Al atoms reached a constant distribution of *CN* species even when increasing the pressure further (up to 24 GPa). Interestingly, instead of focusing on the network formers, the Na^+ sites in a Na_2O-Al_2O_3-$6SiO_2$ (albite) glass under cold compression up to 2 GPa were found to undergo a significant volumetric decrease, in great agreement with the overall change in volume upon pressure increase [22].

Other important classes of mixed former glasses are borosilicates and aluminoborates. For both families, NMR has been the golden standard for probing local order as it allows for easily accessing coordination states of Al, B, and Si. This includes structural characterization of hot-compressed (up to 2 GPa) soda lime borosilicate (in the $15Na_2O$-$10CaO$-xB_2O_3-$(100-x)SiO_2$ series) glasses to access the CN of boron, generally finding a larger relative increase of boron CN upon hot compression for boron-poor compositions but larger plastic compressibility (i.e., relative density change) for boron-rich compositions [73]. Another study on hot-compressed calcium-aluminoborosilicate glasses found that compositions with higher concentration of boron shows higher recoverable densification [74]. Similarly, two commercial borosilicates (Schott N-BK7® and Borofloat33®) were hot-compressed and studied by ^{11}B NMR as well as MD simulations, finding angular alteration and boron coordination changes to be the dominant densification mechanisms [75]. The same mechanisms were observed in simulated cold compressed commercial Schott N-BK7® and Borofloat33®

glasses [76]. In the aluminoborate family, the main interest has been on their pronounced property changes upon hot compression due to their highly adaptive network structure, as both Al and B are prone to change CN in this pressure range (unlike Si). For a $24Li_2O$-$21Al_2O_3$-$55B_2O_3$ glass, hot compression at 2 GPa significantly increased the Al and B CNs and altered the mechanical properties [9,21]. This is interesting, given how cold compression showed only negligible effects on Al CN after pressure release in an aluminosilicate glass in this pressure regime [72] and it thus highlights the possible uses of hot relative to cold compression.

Only relatively few pressure studies have been performed on phosphate-based glasses. Generally, phosphate glasses have been found to only exhibit changes of Q^n speciation upon hot compression, while Al in aluminophosphates features qualitatively the same increase in CN upon hot compression as in other oxide glass formers [77]. Notably, in a $50ZnO$-$50P_2O_5$ glass, an interesting network depolymerization upon increasing pressure was reported [78]. This highlights the complex interaction between the network-forming phosphate units and the network-intermediate Zn^{2+} cations. Also recently, an even more complex modifier-free Al_2O_3-B_2O_3-P_2O_5-SiO_2 glass family was studied by NMR and Raman spectroscopy, finding complex interactions between formers and their response to hot compression. This allowed for tuning the conversion of B^{III} to B^{IV} and the local ring-type structures through compositional design and pressure treatment [79,80].

3.5 Other network formers

In the above, we have highlighted the structural pressure studies on glasses with the most common oxides, but there is also an increasing interest in studying glasses with more exotic (non-traditional) oxides. A recent example is that of amorphous TiO_2, which can be formed through a pressure-driven crystal-to-amorphous transition at pressures above ~13 GPa [81]. Studying this system up to ~86 GPa of cold compression showed an increase in the Ti-O CN from 7 at ~16 GPa to 9 at ~86 GPa, which involved a direct transition from a 7- to a 9-fold coordinated state. This is consistent with results for crystalline analogues, yet in somewhat disagreement with *ab initio* MD simulations predicting a mean CN of 8 at approximately 80 GPa, yet with the presence of both 7-, 8- and 9- fold coordinated Ti atoms [82]. Another example is that of a $20BaO$-$80TeO_2$ glass, which was studied *in situ* at high pressure at room temperature using neutron diffraction [27]. For the network former, Te, the average coordination number was found to increase from ~3.51 to ~3.73, with similar

trends reported for the remaining atomic types (Ba and O). Such increasing connectivity was also suggested by Raman spectroscopy measurements [27]. Interestingly, this highlights that the Te network-former may adapt its SRO structure at much lower pressures compared to that of other oxide species (Fig. 5), but we note that further measurements are needed to reveal its ultrahigh pressure response.

4. Glass Properties

4.1 Density

The most obvious consequence of the structural changes discussed in the previous section is the volumetric densification of the glass. In terms of volumetric changes, the pressure-volume behaviors of oxide glasses are largely dependent on the chemical composition. For instance, silica exhibit two regions in the pressure-volume relationship, i.e., elastic regime under compression up to $0.82V/V_0$, and plastic region under compression starting from $0.82V/V_0$, corresponding to an irreversible compaction with pressure over 10 GPa [83]. The degree of densification is typically calculated as density increase upon compression ($\Delta\rho$) relative to the initial density (ρ_0) [84] or similarly by the irreversible plastic compressibility ($\beta = -(1/V)(dV/dP)$), where V is the initial volume of the glass before compression, dV is the volume change measured *after* decompression to ambient conditions, and dP is the applied pressure [85]. It is observed in glasses that the density increase with pressure reaches an upper limit, after which further pressure increase leads to only a minor increase in density (Fig. 7a). However, we note that not all high-pressures setups described in Section 2 can generate sufficiently high pressure to reach this saturated plateau. Figure 7b shows that the maximum density change after high-pressure treatment decreases with increasing Poisson's ratio of the ambient pressure glass. The glasses with open structures such as silica and germania have a high polymerization degree, making them resistant to contraction in the transverse direction upon tension, and thus exhibit a low Poisson's ratio (<0.2). In contrast, bulk metallic glasses exhibit a close-packed atomic network, facilitating atomic movement in the transverse direction upon tension, and thus feature higher Poisson's ratios (~0.38).

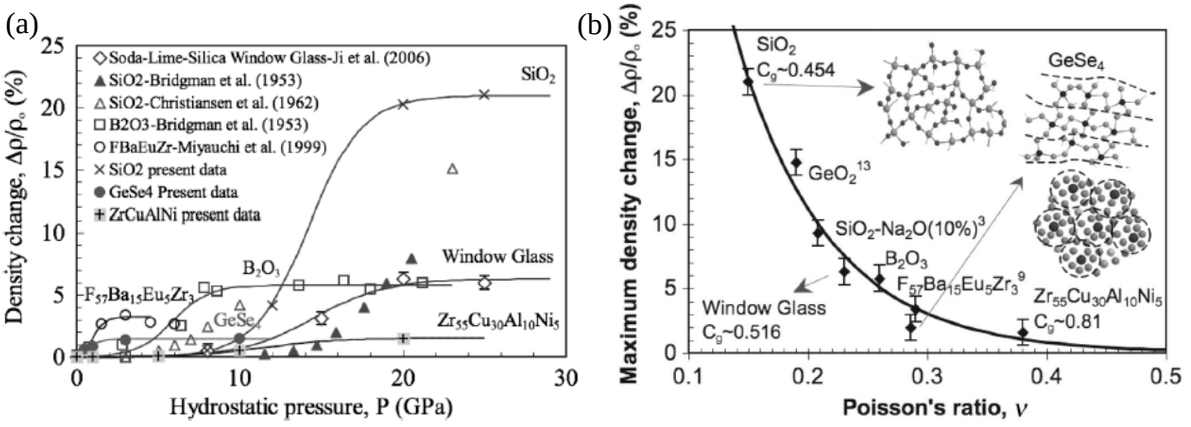

Figure 7. Densification of glasses. (a) Density change as a function of the applied pressure at room temperature [84]. (b) Maximum density change as a function of Poisson's ratio [86]. (a) and (b) are reproduced with permission from Rouxel *et al.*, *Phys. Rev. Lett.* **2008**, *100*, 225501. Copyright 2008 The American Physical Society.

4.2 Elastic moduli

Elastic moduli are important material properties that describe the resistance to elastic deformation. The effect of pressure on elastic moduli (except Poisson's ratio) of most oxide glasses has been found to have a positive correlation and to also be sensitive to the temperature used for compression [10]. For example, it was found that elastic moduli of hot-compressed mixed-alkali (K_2O/Na_2O) aluminosilicate glasses showed only a small mixed alkali effect comparing to that observed in the as-prepared glasses [87]. Deschamps et al. [28] studied elastic moduli changes of pressurized silica glass as measured by Brillouin spectroscopy after decompression to ambient from cold compression in a DAC. The longitudinal sound velocity and therefore elastic moduli were found to exhibit an anomalous behavior, showing a decrease for $\Delta\rho/\rho_0 < 5\%$ (i.e., <12 GPa) and an increase for $\Delta\rho/\rho_0 > 5\%$ (i.e., >12 GPa). The authors further concluded that the elastic moduli do not depend on the compression path experienced by the glass to reach the permanent densification. Guerette et al. [68] also studied the elastic moduli changes of silica glass under both hot and cold compression and found a contradictory result from that of Deschamps et al. [28]. In the latter study, the elastic moduli were found to depend on both the extent of densification and the pathway to reach the permanent densification of the silica

glass. The silica glass from hot-compression had higher bulk modulus than that from the cold-compression for the same extent of densification below 20%. However, this difference became smaller when the extent of densification was above 20%. Molecular dynamics simulations in the same study showed how the MRO structure of the hot-compressed and cold-compressed silica glasses was different, explaining the differences in the elastic properties.

For small degrees of densification ($\Delta\rho/\rho_0 < 2\%$), compressed silica glass seems to have the same elastic moduli as that of the pre-compressed one, but when $\Delta\rho/\rho_0 > 2\%$, the elastic moduli increase significantly upon densification [28]. This increase agrees well with that observed elsewhere [88] in the case of Young's, bulk, and shear moduli. For these three elastic moduli, an approximately linear relationship with the plastic compressibility was observed, implying that the elastic moduli change in compressed glasses is governed by the overall degree of network densification, which in turn is a combined effect of changes in SRO and MRO. Figure 8a shows this relation for a larger range of glasses, although the trend is less clear with the extended composition ranges. The pressure-induced changes in Poisson's ratio, unlike those in Young's modulus, of oxide glasses do not always show the positive impact upon densification. In compressed soda-lime-silica, lithium aluminoborate, and sodium borosilicate glasses, Poisson's ratio decreases with increasing pressure [21]. This decrease was found even for the extent of densification of around 15%, which is contrary to the case of compressed silica glass in Ref. [28]. Figure 8b shows the lack of a clear relation between the extent of densification and the pressure-induced change in Poisson's ratio.

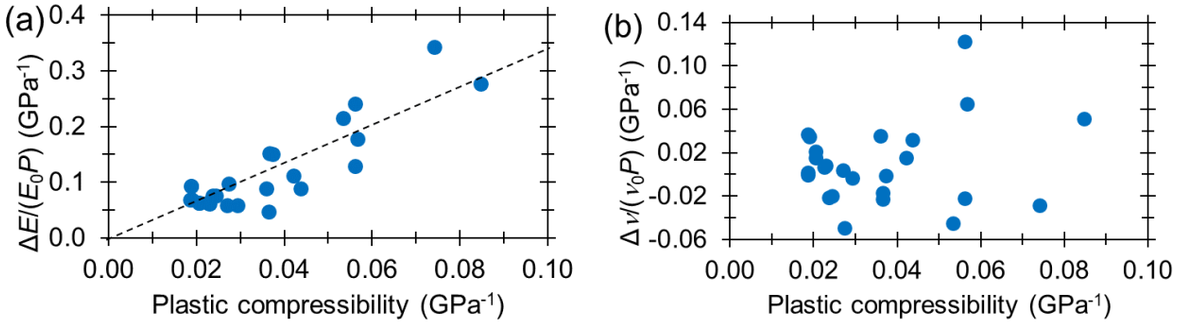

Figure 8. The normalized change in Young's modulus (a) and Poisson's ratio (b) as a function of plastic compressibility for hot-compressed oxide glasses. Panel (a) was reproduced from [88] with extended data from [21,87,89]. Data for panel (b) was taken from Refs. [23,28,88]. The dashed line in (a) is taken from Ref. [88].

4.3 Indentation hardness

Indentation, typically done using a Vickers tip at ambient conditions, is a means of applying a sharp contact load on the surface of glass, which can also produce hydrostatic stresses. Therefore, it is important to perform high-pressure experiments to understand the inelastic deformation mechanisms that occur during the indentation testing in order to design glasses with improved resistance toward deformation and damage upon such sharp contact loading that also happens in real-life applications. As discussed in Section 3, the structure of glasses changes under high-pressure treatment, resulting in direct changes in mechanical properties such as hardness as it is well known that hardness is sensitive to the local bonding and atomic packing behavior [90].

An indentation study on a hot-compressed lithium aluminoborate glass showed that Vickers hardness (H_V) and density exhibit the same pressure dependence [9]. The relative increases in H_V (70%) and density (12%) were the highest values reported for any hot-compressed oxide glass. The high-pressure-induced changes in these properties are related to the increases of packing density and number of atomic bonds per unit volume, adding to the increase of the coordination numbers, e.g., the changes from B^{III} to B^{IV}. This study agreed well with a previous study on soda-lime-borate glasses [91], which showed that the pressure-induced increase in hardness is higher in glasses with greater plastic compressibility, i.e., glasses with higher content of B^{III} is easier to densify than those with lower B^{III} because B^{III} transforms to B^{IV} upon compression. Another study on sodium aluminoborate glasses also supported these findings [92].

Different glass network formers appear to have different effects on the Vickers hardness increase upon compression. Januchta et al. [89] studied the pressure-induced changes in H_V of lanthanum aluminoborate, aluminosilicate, and aluminogermanate glasses with the same molar fractions of La_2O_3 and Al_2O_3. The borate glass had the largest change in H_V, likely due to its more pronounced structural changes upon compression. Indeed, Raman maps on the bulk and Vickers indented areas of the as-prepared borate glass shows that this glass network experiences a significate change upon indentation (compression), whereas that of the silicate

glass remains unchanged. The network of germania glass changes only to a small extent upon indentation, explaining why the hardness of the hot-compressed glass increases very slightly. The relationship between glass network and hardness changes upon densification was also reported in the study of hardness of lithium aluminoborate, soda-lime-silicate and sodium borosilicate glasses [21]. Among the three glasses, the aluminoborate glass had the highest pressure-induced increase in H_V. Finally, we note that unlike the pressure-induced changes in elastic moduli, those in hardness do not eliminate the mixed alkali effect upon compression, but, instead, tend to increase it, e.g., in the case of sodium/potassium aluminosilicate glasses [87].

4.4 Crack resistance

Crack resistance (CR) or crack initiation resistance is defined as the indentation load at which the probability for forming the indentation corner cracking is 50%. CR is a surface property that depends strongly on the surface roughness, the loading and unloading rate, and the measurement atmosphere, etc. It is thus not an intrinsic property such as fracture toughness (K_{Ic}). A relationship between the extent of densification and CR, i.e., CR decreases with increasing the extent of densification, has been reported in many studies. In fact, it has been reported that the densification ratio is an important factor for CR [8]. Permanent densification can dissipate the mechanical energy induced by the indentation, resulting in less driving force for cracking in glass. This can likely explain the decrease in CR upon compression of glasses as they become denser with less ability to dissipate the energy through further densification [9]. Furthermore, Figure 9 shows the CR as a function of the $[K_2O]/([Na_2O]+[K_2O])$ ratio in as-prepared and compressed mixed potassium/sodium aluminosilicate glasses [87]. CR decreases with increasing pressure. Moreover, similarly to the elastic moduli, it is noteworthy how the mixed alkali effect becomes smaller at higher pressure.

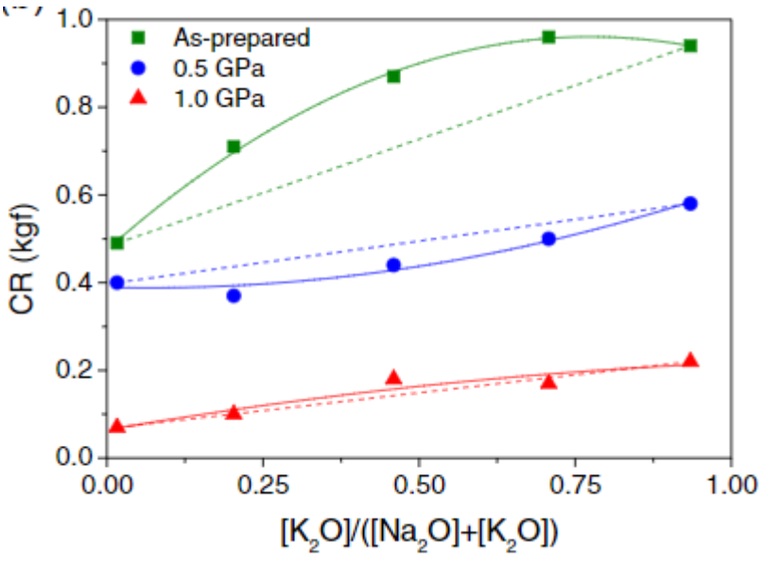

Figure 9. Mixed alkali effect on crack resistance (CR) of potassium/sodium aluminosilicate glasses before and after hot-compression at 0.5 and 1 GPa. The figure is reproduced with permission from Aakermann *et al.*, *J. Non-Cryst. Solids.* **2015**, *426*, 175-183. Copyright 2015 Elsevier. [87].

4.5 Fracture toughness

Fracture toughness (K_{Ic}) is the resistance to rapid crack extension and depends on the elastic moduli and fracture energy (G_C). As described in Section 4.2, the elastic moduli increase with increasing pressure and the glass becomes denser leading to the increase of connectivity. Consequently, compression should also lead to an increase in K_{Ic}. Figure 10 shows the relationship between the normalized pressure-induced change in K_{Ic} and the plastic compressibility of three hot-compressed oxide glasses, i.e., soda-lime-silicate, lithium aluminoborate and sodium borosilicate glasses [21]. In these glasses, the elastic moduli as well as fracture energies also increase with increasing extent of densification. Another recent study based on MD simulations of two commercial borosilicate glasses (Boro33 and N-BK7) also shows the importance of the degree of densification on fracture toughness [93]. Boro33 has a higher amount of B^3 and exhibits a better densification upon compression, resulting in a larger increase in K_{Ic} upon compression relative to the case of N-BK7. As such, it is important to design glasses with a high extent of densification in the search for high-fracture toughness oxide glasses.

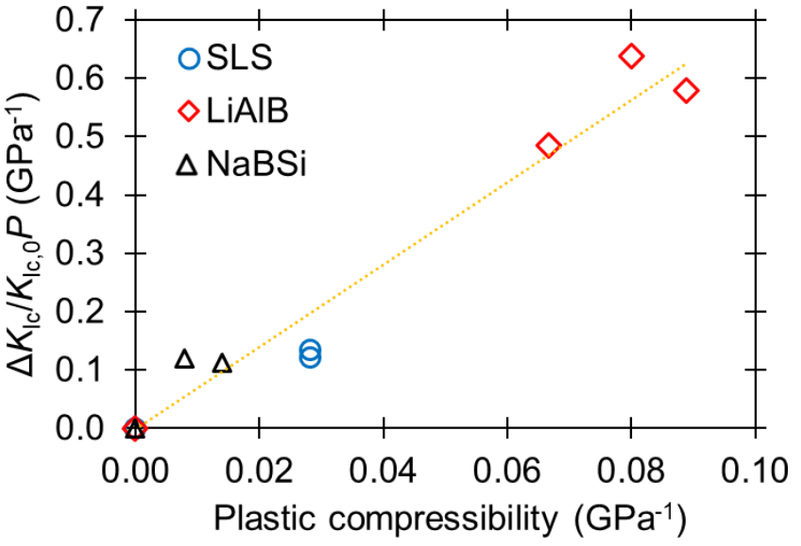

Figure 10. Normalized pressure-induced change in fracture toughness (K_{Ic}) as a function of the plastic compressibility. Both values represent the pressure-induced change relative to the as-prepared glass. The data are taken from [21]. The yellow dash line is a guide for the eye. SLS, LiAlB and NaBSi represent soda-lime-silica, lithium aluminoborate, and sodium borosilicate glasses, respectively.

4.6 Optical properties

Optical properties are important for many oxide glass applications, from float glass in building windows to communication applications. In the latter application, silica glass is an indispensable candidate; however, the transmission loss of silica glass is a major problem. A study on transmission of silica glass showed that the shrinkage of structural voids by hot compression is a promising way to decrease the transmission loss [94]. By hot-compression at 200 MPa and 1800 °C for 4 h, the Rayleigh scattering loss decreased by a factor of two compared to the as-prepared glass. Another simulation study on silica glass also showed the advantages of compression on the reduction of the Rayleigh scattering [95]. The study investigated the atomistic origin of the pressure effect on the shrinkage of the structural voids of compressed silica glass. That is, upon 4 GPa compression, the compressed glass reduced its maximum void size from 0.25 to 0.17 nm, and its Rayleigh scattering loss by more than 50% relative to the as-prepared glass.

5. Emerging paradigms and methods for structural characterization

As described in the previous sections, oxide glasses undergo structural changes upon compression that impact their macroscopic properties. In this section, we will mainly focus on topological analysis tools for analyzing the MRO structure of densified glass materials. Based on these novel methods, new insights into the densification mechanism of oxide glass have been made in the past few years.

5.1 Structural homogeneity

The structure extending beyond the first coordination shell, commonly denoted as MRO structure, can influence various properties and structural differences between cold- and hot-compressed glasses are often present at MRO length scales [68]. However, MRO remains less well understood relative to SRO structure given the lack of usable experimental techniques for probing this structural regime. A few recent studies have been devoted to understanding the changes of MRO in cold- and hot-compression of glassy SiO_2 [68]. Specifically, while arguing for having a compacted yet still fully tetrahedral network at pressures up to ~8 GPa (as expected in this pressure range [38,68]), the observed mechanical properties differ significantly between cold- and hot compressed samples. Based on diffraction and Raman measurements as well as molecular dynamics (MD) simulations, this observation is ascribed to a persistent presence of structural "pores" upon cold compression, while such pores are absent upon hot compression [68].

The effects of pressure, especially on mechanical properties, have later been shown to be more pronounced for hot-compressed than cold compressed SiO_2 glasses. This effect is ascribed to a larger degree of structural homogeneity in the former [68,69], analogous to the effect of differences in local homogeneity observed in borates under pressure (Section 3.3). Interestingly Raman and X-ray scattering studies on both cold and hot compressed SiO_2 glasses suggest the existence of a non-linear structural relaxation process for densified silica, and hence arguing for the existence of more than a single basin in its energy landscape [96,97]. Another perspective on polymorphism in glassy SiO_2 is based on a semi-empirical *ab initio* method by identifying so-called 'percolation transitions', namely "infinite" chains of alike polyhedra that continuously

exchange, ultimately governing the macroscopic properties of silica [35]. Interestingly, this new analytical tool can, e.g., account for the well-known pressure vs. bulk modulus anomaly in glassy silica [98]. Moreover, the percolation probability may be seen as a means of describing transitions between different isochemical amorphous phases and bears resemblance to the polymorphism found in, e.g., amorphous ice phases [99].

5.2 Ring statistics

The MRO structure of oxide glasses is often described by the presence of ring structures, i.e., loops enclosed by chemical bonds. The ring structures can be defined through the following criteria: shortest path, strong rings, and primitive (or irreducible) rings. Although the ring statistics is an important structural feature in glass materials, most of such information are obtained by atomistic simulations since this structural feature is hard to obtain by conventional experimental techniques. The primitive ring distributions in different structures of SiO_2 crystals and glass are shown in Fig. 11 [100]. Note that here the ring size is defined by the number of Si atoms in a ring. α-cristobalite only consists of 6-fold rings, while α-quartz mainly has 8-fold rings with a smaller number of 6-fold rings. Coesite and SiO_2 glass both exhibit a distribution of different size rings, however, the distribution in SiO_2 glass is centered at a ring size of 6 while coesite has multiple peaks. Although all the crystalline forms of SiO_2 have corner-sharing tetrahedral motifs, the distribution of ring statistics exhibits an increasing disorder with increasing density (2.91 g/cm^3 of coesite > 2.66 g/cm^3 of α-quartz > 2.33 g/cm^3 of α-cristobalite).

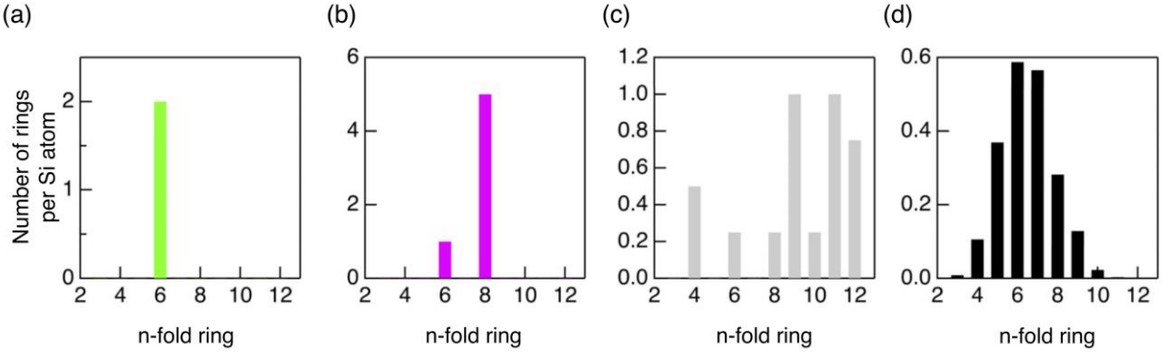

Figure **11**. Distribution of primitive ring size in (a) α-cristobalite, (b) α-quartz, (c) coesite, and (d) glassy SiO_2. Reproduced from Onodera *et al., J. Ceram. Soc. Japan* **2019**. 127, 853 under open access license. [100]

The atomistic densification mechanism of SiO_2 glass upon cold compression can be explained through the 'zipper' model, i.e., ring closure events induced by high pressures [32]. This model describes the corresponding dependence of mean primitive ring size $\langle n \rangle$ and *CN* of Si atom which follows: $\langle n \rangle \cong [4\langle n_0 \rangle + 2(CN - 4)] \,/\, CN$, where $\langle n_0 \rangle$ is the ambient mean primitive ring size. The mean primitive ring size is calculated by $\langle n \rangle \equiv \sum n\ell_n \,/\, \sum \ell_n$, where ℓ_n is the number of rings consisting of a total number *n* of Si and O atoms. Figure 12 shows a schematic of two ring closure events. Before a ring closure event (Fig. 12a), a ring structure with a typical size of 12 is comprised of corner-sharing tetrahedra, i.e., each Si atom is connected to four bridging oxygens. After the first ring closure event (Fig. 12b), one four-fold coordinated Si atom is transitioned into a five-fold coordinated Si atom, which is connected to four bridging oxygen and one threefold coordinated oxygen atom. The second ring closure event initiates with a further increase of pressure, leading to the formation of a second five-fold coordinated Si atom (Fig. 12c). The coordination change and $\langle n \rangle$ dependences on pressure are shown in Fig. 12-e, indicating the correlation between the formation of high-coordinated (5-coordinated or more) Si atoms and ring closure as proposed by the 'zipper' model.

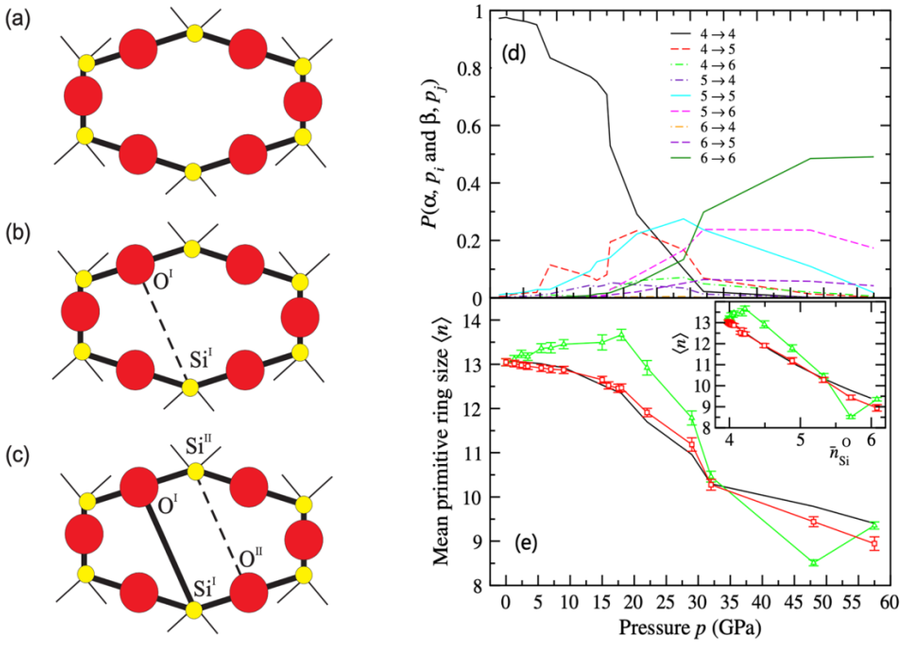

Figure 12. (a-c) Schematic of the "zipper" model of ring closure events in silica glass induced by high pressure: (a) initial ring with 12 atoms, (b) ring after the first single closure event, and (c) ring after the second closure event. Si atoms and O atoms are colored in yellow and red, respectively. The connection of the Si-O bonds is represented by black lines. (d) Pressure dependence of the probability of Si-O coordination number changes. (e) Pressure dependence of the primitive ring size changes from cold-compression simulation (red square), melt-quench simulation (green triangle) and "zipper" model prediction (black). The inset presents the mean primitive ring size as a function of Si-O coordination. Reproduced with permission from Zeidler *et al.*, *Phys. Rev. Lett.* **2014**, *113* (13), 135501. Copyright 2014 American Physical Society.

Recently, it has been reported that the ring size distribution of silicate glass is hidden in the shape of the first sharp diffraction peak (FSDP), which makes it possible to characterize the ring statistics solely through neutron diffraction measurements by using the so-called RingFSDP method [101]. The rings with different sizes exhibit different contributions to the FSDP in the structure factor. Therefore, the fraction of three groups of rings (i.e., ≤4-membered, 5-membered, and ≥6 membered) can be determined through the deconvolution of the FSDP in the experimental neutron structure factor. Based on the neutron and X-ray diffraction patterns of B_2O_3 glass, the position and shape of FSDP both change significantly with increasing pressure. Specifically,

the height of the FSDP decreases while its position exhibits an almost linear increase as the pressure is increased from ambient to 8.5 GPa, indicating a MRO structural transformation upon densification (i.e., the decomposition of boroxol rings) [102]. Finally, we note that Raman spectroscopy is an interesting experimental probe for characterization of small rings (3-4 Si) in silica [103,104], although such methods still largely rely on interpretation of spectral features in the obtained Raman spectra.

5.3 Cavity analysis

Apart from rings of atoms, the presence of empty regions, i.e., cavities, plays an important role in governing the physicochemical properties of glasses. The transformation between crystalline and glassy phases [105] as well as the densification process under pressure [106] can be reflected through the changes in the cavities. Although techniques such as positron annihilation lifetime spectroscopy (PALS) can be used to directly characterize the behaviors of cavities [107], additional insights can be obtained by calculating the distribution of cavities based on the atomic configurations from MD simulations. On the basis of different algorithms, several packages have been developed to identify the distribution of cavities in both crystalline and disordered materials [108,109]. As an example, the transition of SiO_2 glass from a low-density to a high-density phase is accompanied by a significant reduction in cavity volumes [106]. However, since the cavity volume calculation depends on the algorithm as well as the definition of the minimum cavity size, the calculated cavity volumes are usually used for qualitative comparison and are difficult to directly compare with experimental results.

5.4 Persistent homology analysis

Even though ring statistics and void analysis have provided important characterization of many glasses, they commonly depend on a variety of user-based input. As an alternative, persistent homology, a type of topological data analysis, has recently been applied to understand glass structure [110]. Persistent homology is used to characterize multiscale topological features based on the coordinates of particles. These topological features can be extracted as n-dimensional holes: $n = 0$ represents connected components (i.e., particles are connected by each other), $n = 1$ represents loops, and $n = 2$ represents cavities. The mostly used tool in persistent homology, the persistence diagram of loops, is built by the following three steps as shown in Fig.

13 [111-113]. First, each atom is replaced by a ball with radius defined by its atom type. The radius of each particle will then be allowed to increase continuously with the same increment. Second, when a pair of growing balls starts to intersect, there will be an edge between the corresponding two balls. Third, the incremented radius at which an additional edge gives rise to a closed loop represents the "birth" of the loop, while the radius at which the loop starts to be filled is the "death" of the loop. The persistence diagram consists of all the "birth" and "death" values (*b*, *d*) and can be used to study the topological properties. The persistence value (*d*-*b*) represents the "lifetime" of the loop, i.e., a large persistence indicates a robust loop.

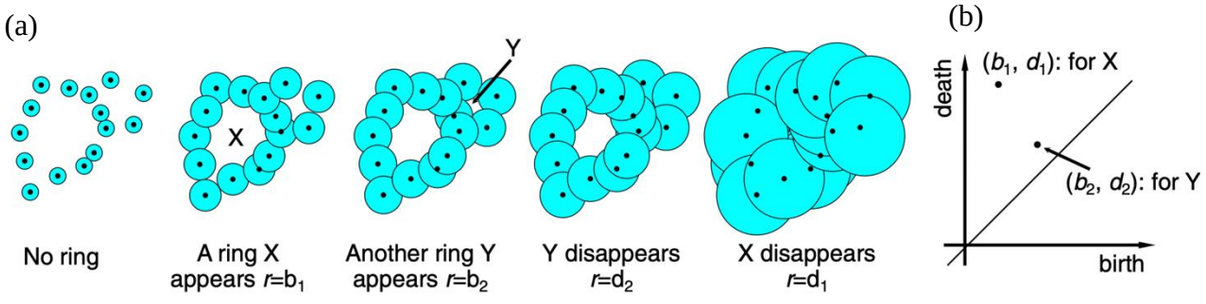

Figure 13. Schematic of the generation of 1-dimensional persistence diagram. (a) Growing atomic balls and (b) corresponding persistence diagram. The initially large and smalls balls represent O and Si atoms, respectively. Reproduced from Onodera *et al. NPG Asia Mater.* **2019**, 11(1), 75 under open access license.

Unlike the conventional structural parameters such as cavity or ring analysis which only focus on specific parts of the glass structure, persistent homology can provide a global perspective on the system by taking all the atoms into account, including the connections and MRO that are not covalently bonded. While there will be a small number of isolated clusters in the persistence diagram of crystalline solid, the clusters become spread and overlapping in the persistence diagrams of isochemical disordered structures [114]. For oxide glasses, the characteristic regions in the persistence diagram of loops indicate the existence of MRO. Given the power in describing the hierarchical structure of glass materials, persistent homology can also reflect the structural origins of mechanical properties. As reported by Hiraoka et al. [112], the curves or islands only exist in the persistence diagrams of the solid materials, indicating these structural features are correlated with the rigidity of solids. Upon deformation, the shape or position of these curves or islands in the persistence

diagrams will also change accordingly [112]. Recently, a better understanding of the MRO structure (especially the origin of the first sharp diffraction peak in the structural factor) has been achieved through deconvoluting the contributions of different regions in the persistence diagrams [111]. These advantages of persistent homology in characterizing MRO enables a better and less biased description of geometrical features in disordered materials as compared to previously used methods. As shown in Fig. 14, the persistence diagrams of loops capture the changes in ring structure of SiO_2 with varying densities in both glassy and crystalline states well. Upon densification, the distribution of geometrical features shift towards lower death values and becomes more concentrated as in the pyrite-type crystalline phase, indicating the transition from network structure to dense-packed structure with an increase in density [37].

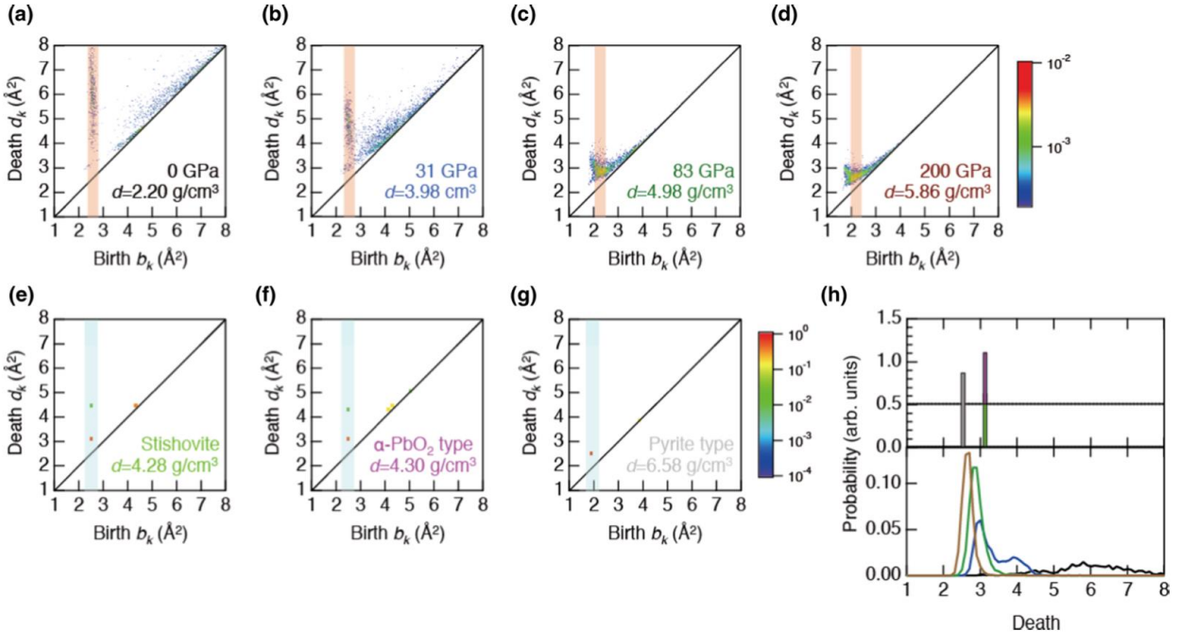

Figure 14. (a-d) Si-centric persistence diagrams at dimension-1 (loops) of SiO_2 glasses at 0, 31, 83, and 200 GPa. (e-g) Si-centric persistence diagrams of stishovite, α-PbO_2-type, and pyrite-type SiO_2. (h) The probability profiles of points along the color bands shown in persistence diagrams above. SiO_2 glasses at 0, 31, 83, and 200 GPa are black, blue, green, and brown lines, while stishovite, α-PbO_2-type, and pyrite-type SiO_2 are green, pink, and gray bars. The top color bar represents Figs. (a)-(d) while the below color bar applies to Figs. (e)-(g). Both color bars represent probability. Reproduced with permission from Murakami *et al.*, *Phys. Rev. B* **2019**, 99, 045153 (2019). Copyright 2019 American Physical Society.

Based on the analysis of persistence diagrams of densified SiO_2 glasses, the geometrical information of SiO_2 glass at 200 GPa is very close to the pyrite-type crystal counterpart. Specifically, the isolated clusterlike "island" in the persistence diagrams at 200 GPa apart from the original broad distribution is very similar to the topological features of metallic glass with highly dense-packed structure. This indicates that the densification of silica glass is achieved by a gradual transition from the network structure to a dense-packed structure through the change of coordination state of individual atoms [37]. Additionally, the increase in the correlation length with coesite-like coordinates in the persistence diagrams indicates the likely precursors to crystal growth in the densified glass [106]. Persistent homology thus offers a new way to rethink the mechanism of glass-to-crystal transition, which should also be helpful to understand the processes of nucleation and crystallization.

6. Outlook

As we have discussed herein, a variety of high-pressure experiments and simulations have been done on oxide glasses. With this work, it is becoming evident that compression can be used as a powerful glass processing technique to tailor the material properties. This includes pressure-induced changes in most physical, mechanical, and optical properties and can be used in the search of denser, harder, stiffer, and tougher materials. Ultimately, a better control of such properties through densification requires a deeper understanding of the structural changes induced by the pressure treatment. However, while glass structure can now be studied *in situ* at high pressure, this is not yet possible for most mechanical properties and there is therefore an ongoing interest in developing high pressure facilities that allow for more *in situ* characterization. In any case, several fundamental questions remain regarding the densified glass structure. This includes the identification of structural descriptors (or fingerprints) that can unify the structural response to pressure among different network forming glasses.

As discussed in Section 3.1 the oxygen packing fraction has attracted recent interest due to its ability to account for pressure-related coordination number changes between the common network glasses (SiO_2, GeO_2, B_2O_3, see Fig. 5a) in some pressure regimes. However, this model is highly dependent on radii

assumptions and problems arise when accounting for very high coordination numbers, e.g., as generated in recent ultrahigh pressure experiments (see Fig. 5b). Another recent approach for glasses is to couple the ratio of the radii of the cation and anion through the ionic radii ratio ($\gamma = r_{\text{cation}} r_{\text{Oxygen}}^{-1}$) for describing the pressure-induced increase in *CN* [81]. This idea has been applied to crystalline materials for decades [115], but show remarkable unification of amorphous and crystal polymorphs of SiO_2, GeO_2, and TiO_2 as presented in Fig. 15. Notably, and in contrast to the use of the oxygen packing fraction in Fig. 5b, there seems to exist notable correlations between crystalline polymorphs and the continuous transitions of the amorphous states, even at very high cation coordination numbers. Extending the presented data to an "ideal" $\gamma = 1$ structure, we would expect a coordination number of 12 [14], in somewhat good agreement with the trend of increasing *CN* with increasing γ in Fig. 15. It will be of great interest in future work to clarify whether modified oxides as well as mixed network former glasses follow the same master curve.

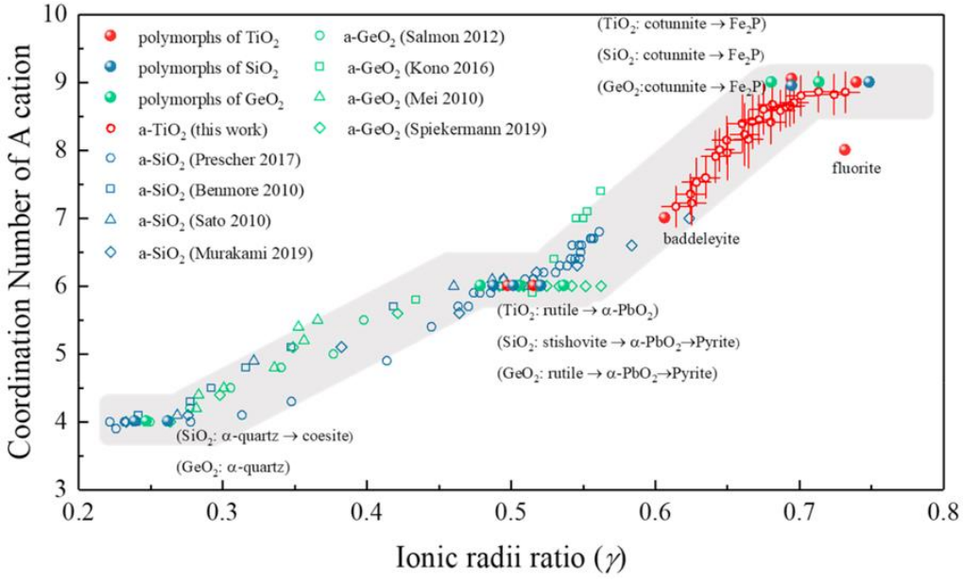

Figure 15. Comparison of ionic radii ratio ($\gamma = r_{\text{Si,Ge,Ti}} r_{\text{O}}^{-1}$) with the cation coordination number of amorphous and crystalline polymorphs of SiO_2, GeO_2, and TiO_2, showcasing a strong correlation, even for very high coordination numbers [81]. The grey-shaded area serves as a guide for the eye. Reproduced with permission from Shu *et al.*, J. Phys. Chem. Lett. **11**, 374 (2020). Copyright 2019 American Chemical Society.

Substantial efforts have been devoted to understanding SRO structure and its response to extreme pressures in both single network former as well as modified glasses. Such studies have been promoted by advances in resolution of measurement techniques, probing new glass compositions and families, or applying higher pressure. The changes in MRO upon densification not only highlights the out-of-equilibrium nature of the glass materials, but also encodes the origin of the low-to-high density transition under pressure [32]. However, the quest for understanding MRO remains much harder to tackle given the few available techniques that all provide data with debatable interpretations. Yet, the growing availability of high-pressure datasets (e.g., from diffraction and spectroscopy techniques) coupled with computational methods (e.g., reverse Monte Carlo, MD simulations, or mixtures hereof [116]) should allow new insights at this structural length scale. For instance, the RingFSDP method [101] offers an experimental approach to characterize the ring size distribution from neutron diffraction patterns, which can potentially be used to understand the ring structure changes in the glass upon densification. Furthermore, with the development of new methods for describing MRO structure, such as those based on machine learning and topological data analysis [111,112], previously overseen correlations may be revealed. Particularly, persistent homology is a promising method for characterizing glass structure, however, the analysis output is difficult to compare directly with experimental data. Such work will likely be supported by advances within, e.g., imaging techniques [117], which have not yet been widely adopted to oxides. Indeed, such methods could ultimately provide the missing link for understanding MRO in this class of densified materials, e.g., in relation to the suggested inhomogeneity in even single oxide glass formers, with notable pressure dependencies [68,69]. Overall, densification treatment appears as an important tool to alter a variety of properties of disordered materials [118,119], and we believe that a deeper understanding into the densification-induced property changes will further broaden the applications of disordered materials.

Acknowledgements

This work was supported by the Independent Research Fund Denmark (0136-00011B). T.D. acknowledges funding for a Marie Skłodowska-Curie Individual Fellowship (101018156).

References

1. A. K. Varshneya, J. C. Mauro, *Fundamentals of Inorganic Glasses* (Elsevier, 2019).
2. P.W. Bridgman, I. Šimon, J. Appl. Phys. 24, 405 (1953).
3. J.D. Mackenzie, J. Am. Ceram. Soc. 46, 461 (1963).
4. D. Machon, F. Meersman, M. C. Wilding, M. Wilson, P. F. McMillan, Prog. Mater. Sci. 61, 216 (2014).
5. J. Kieffer, J. Non-Cryst. Solids 307-310, 644 (2002).
6. O. Mishima, Y. Suzuki, Nature 419, 599 (2002).
7. K. Januchta, M. M. Smedskjaer, J. Non-Cryst. Solids X 1, 100007 (2019).
8. S. Yoshida, J. Non-Cryst. Solids X 1, 100009 (2019).
9. K. Januchta, R.E. Youngman, A. Goel, M. Bauchy, S.L. Logunov, S.J. Rzoska, M. Bockowski, L.R. Jensen, M.M. Smedskjaer, Chem. Mater. 29, 5865 (2017).
10. S. Kapoor, L. Wondraczek, M. M. Smedskjaer, Front. Mater. 4, 1 (2017).
11. M. R. Cicconi, D. R. Neuville, "Natural Glasses," in: *Springer Handbook of Glass* (Springer Nature, 2019, eds. J. D. Musgraves, J. Hu, L. Calvez) pp. 771-812.
12. P. S. Salmon, A. Zeidler, J. Phys.: Condens. Matter 27, 133201 (2015).
13. S. Kohara, P. S. Salmon, Adv. Phys. X 1, 640 (2016).
14. P. S. Salmon, L. Huang, MRS Bull. 42, 734 (2017).
15. S. Klotz, J. C. Chervin, P. Munsch, G. J. Le Marchand, J. Phys. D: Appl. Phys. 42, 075413 (2009)
16. H. Huppertz, Z. Kristallogr. Cryst. Mater. 219, 330 (2004).
17. S. Yoshida, J.-C. Sanglebæuf, T. Rouxel, J. Mater. Res. 20, 3404 (2005).
18. M. Stepniewska, K. Januchta, C. Zhou, A. Qiao, M. M. Smedskjaer, Y. Yue, Proc. Natl. Acad. Sci. U.S.A. 117, 10149 (2020).
19. D. Walker, M. A. Carpenter, C. M. Hitch, Am. Mineral. 75, 1020 (1990).
20. T. Sato, N. Funamori, T. Yagi, Nat. Commun. 2, 345 (2011).
21. T. To, S. S. Sørensen, J. F. S. Christensen, R. Christensen, L. R. Jensen, M. Bockowski, M. Bauchy, M. M. Smedskjaer, ACS Appl. Mater. Interfaces 13, 17753 (2021).

22. S. J. Gaudio, T. G. Edwards, S. Sen, Am. Mineral. 100, 326 (2015).
23. P. T. T. Wong, D. D. Klug, Appl. Spectro. 37, 284 (1983).
24. C. S. Zha, J. S. Tse, W. A. Bassett, J. Chem. Phys. 145, 124315 (2016).
25. C. J. Benmore, E. Soignard, S. A. Amin, M. Guhrie, S. D. Shastri, P. L. Lee, J. L. Yarger, Phys. Rev. B 81, 054105 (2010).
26. G. Morard, J. A. Hernandez, M. Guarguaglini, R. Bolis, A. Benuzzi-Mounaix, T. Vinci, G. Fiquet, M. A. Baron, S. H. Shim, B. Ko, A. E. Gleason, W. L. Mao, R. Alonso-Mori, H. J. Lee, B. Nagler, E. Galtier, D. Sokaras, S. H. Glenzer, D. Andrault, G. Garbarino, M. Mezouar, A.K. Schuster, A. Ravasio, Proc. Natl. Acad. Sci. U. S. A. 117, 11981 (2020).
27. A. Khanna, A. Kaur, Hirdesh, S. Tyagi, N.P. Funnell, C.L. Bull, RSC Adv. 10, 42502 (2020).
28. T. Deschamps, J. Margueritat, C. Martinet, A. Mermet, B. Champagnon, Sci. Rep. 4, 7193 (2014).
29. Y. B. Gerbig, C. A. Michaels, J. Non-Cryst. Solids 530, 119828 (2020).
30. Y. B. Gerbig, C. A. Michaels, A. M. Forster, J. W. Hettenhouser, W. E. Byrd, D. J. Morris, R. F. Cook, Rev. Sci. Instrum. 83, 125106 (2012).
31. V. V. Brazhkin, A.G. Lyapin, K. Trachenko, Phys. Rev. B 83, 132103 (2011).
32. A. Zeidler, K. Wezka, R.F. Rowlands, D.A.J. Whittaker, P.S. Salmon, A. Polidori, J.W.E. Drewitt, S. Klotz, H.E. Fischer, M.C. Wilding, C.L. Bull, M.G. Tucker, M. Wilson, Phys. Rev. Lett. 113, 135501 (2014).
33. J. F. Stebbins, S. Bista, J. Non-Cryst. Solids 505, 234 (2019).
34. T. Sato, N. Funamori, D. Wakabayashi, K. Nishida, T. Kikegawa, Phys. Rev. B 98, 144111 (2018).
35. A. Hasmy, S. Ispas, B. Hehlen, Nature 599, 62 (2021).
36. C. Prescher, V. B. Prakapenka, J. Stefanski, S. Jahn, L. B. Skinner, Y. Wang, Proc. Natl. Acad. Sci. U.S.A. 114, 10041 (2017).
37. M. Murakami, S. Kohara, N. Kitamura, J. Akola, H. Inoue, A. Hirata, Y. Hiraoka, Y. Onodera, I. Obayashi, J. Kalikka, N. Hirao, T. Musso, A.S. Foster, Y. Idemoto, O. Sakata, Y. Ohishi, Phys. Rev. B 99, 045153 (2019).
38. Y. Kono, Y. Shu, C. Kenney-Benson, Y. Wang, G. Shen, Phys. Rev. Lett. 125, 205701 (2020).

39. G. Spiekermann, M. Harder, K. Gilmore, P. Zalden, C.J. Sahle, S. Petitgirard, M. Wilke, N. Biedermann, C. Weis, W. Morgenroth, J.S. Tse, E. Kulik, N. Nishiyama, H. Yavaş, C. Sternemann, Phys. Rev. X 9, 011025 (2019).
40. Y. Kono, C. Kenney-Benson, D. Ikuta, Y. Shibazaki, Y. Wang, G. Shen, A. Navrotsky, Proc. Natl. Acad. Sci. U.S.A.113, 3436 (2016).
41. S.K. Lee, P.J. Eng, H. K. Mao, Y. Meng, M. Newville, M. Y. Hu, J. Shu, Nat. Mater. 4, 851 (2005).
42. S. K. Lee, Y. H. Kim, P. Chow, Y. Xiao, C. Ji, G. Shen, Proc. Natl. Acad. Sci. U.S.A. 115, 5855 (2018).
43. T. Sato, N. Funamori, Phys. Rev. B 82, 184102 (2010).
44. E. Ryuo, D. Wakabayashi, A. Koura, F. Shimojo, Phys. Rev. B 96, 054206 (2017).
45. S.K. Lee, Y.H. Kim, Y.S. Yi, P. Chow, Y. Xiao, C. Ji, G. Shen, Phys. Rev. Lett. 123, 235701 (2019).
46. O'Keeffe M. & Hyde B. G. in *Structure and Bonding in Crystals*, eds O'Keeffe, M. & Navrotsky, A. pp. 227-254 (Academic, 1981).
47. A. Zeidler, P.S. Salmon, L.B. Skinner, Proc. Natl. Acad. Sci. U.S.A. 111, 10045 (2014).
48. X. Du and J.S. Tse, J. Phys. Chem. B 121, 10726 (2017).
49. J.S. Tse, Natl. Sci. Rev. 7, 149 (2020).
50. R. Youngman, Mater. 11, 476 (2018).
51. E.J. Kim, Y.H. Kim, S.K. Lee, J. Phys. Chem. C 123, 26608 (2019).
52. X. Wen, G. Tang, Q. Yang, X. Chen, Q. Qian, Q. Zhang, Z. Yang, Sci. Rep. 6, 20344 (2016).
53. M.K. Murthy, J. Ip., Nature 201, 285 (1964).
54. G. Lelong, L. Cormier, G. Ferlat, V. Giordano, G.S. Henderson, A. Shukla, G. Calas, Phys. Rev. B 85, 134202 (2012).
55. S. Petitgirard, G. Spiekermann, K. Glazyrin, J. Garrevoet, M. Murakami, Phys. Rev. B 100, 214104 (2019).
56. T.T. Duong, T. Iitaka, P.K. Hung, N. Van Hong, J. Non-Cryst. Solids 459, 103 (2017).
57. K.V. Shanavas, N. Garg, S.M. Sharma, Phys. Rev. B 73, 094120 (2006).
58. N.M. Anh, N.T.T. Trang, T.T. Nguyet, N.V. Linh, N.V. Hong, Comput. Mater. Sci. 177, 109597 (2020).
59. J. Peralta, G. Gutiérrez, Eur. Phys. J. B 87, 257 (2014).
60. A. Cornet, R. Molherac, B. Champagnon, C. Martinet, J. Appl. Phys. 120, 115901 (2016).

61. M. Krstulović, A.D. Rosa, N. Biedermann, G. Spiekermann, T. Irifune, M. Muñoz, M. Wilke, Phys. Rev. B 101, 214103 (2020).
62. V. V. Brazhkin, Y. Katayama, K. Trachenko, O.B. Tsiok, A.G. Lyapin, E. Artacho, M. Dove, G. Ferlat, Y. Inamura, H. Saitoh, Phys. Rev. Lett. 101, 035702 (2008).
63. K. Trachenko, V. V. Brazhkin, G. Ferlat, M.T. Dove, E. Artacho, Phys. Rev. B 78, 172102 (2008).
64. T. Edwards, T. Endo, J.H. Walton, S. Sen, Science 345, 1027 (2014).
65. F. Funabiki, S. Matsuishi, H. Hosono, J. Appl. Phys. 113, 223508 (2013).
66. H. Dong, A.R. Oganov, V. V. Brazhkin, Q. Wang, J. Zhang, M.M. Davari Esfahani, X.F. Zhou, F. Wu, Q. Zhu, Phys. Rev. B 98, 174109 (2018).
67. S.K. Lee, A.C. Lee, J.J. Kweon, J. Phys. Chem. Lett. 12, 1330 (2021).
68. M. Guerette, M.R. Ackerson, J. Thomas, F. Yuan, E.B. Watson, D. Walker, L. Huang, Sci. Rep. 5, 15343 (2015).
69. M. Guerette, M.R. Ackerson, J. Thomas, E.B. Watson, L. Huang, J. Chem. Phys. 148, 194501 (2018).
70. M. Krstulović, A.D. Rosa, N. Biedermann, T. Irifune, M. Wilke, Chem. Geo. 560, 119980 (2021).
71. J. Wu, J. Deubener, J. F. Stebbins, L. Grygarova, H. Behrens, L. Wondraczek, Y. Yue, J. Chem. Phys. 131, 104504 (2009).
72. S.K. Lee, K.Y. Mun, Y.H. Kim, J. Lhee, T. Okuchi, J.F. Lin, J. Phys. Chem. Lett. 11, 2917 (2020).
73. S.S. Sørensen, M.S. Bødker, H. Johra, R.E. Youngman, S.L. Logunov, M. Bockowski, S.J. Rzoska, J.C. Mauro, M.M. Smedskjaer, J. Non-Cryst. Solids 557, 120644 (2021).
74. J. Wu, T. M. Gross, L. Huang, S. P. Jaccani, R. E. Youngman, S. J. Rzoska, M. Bockowski, S. Bista, J. F. Stebbins, M. M. Smedskjaer, J. Non-Cryst. Solids 530, 119797 (2020).
75. L. Ding, K.H. Lee, T. Zhao, Y. Yang, M. Bockowski, B. Ziebarth, Q. Wang, J. Ren, M.M. Smedskjaer, J.C. Mauro, J. Am. Ceram. Soc. 103, 6215 (2020).
76. K.-H. Lee, Y. Yang, L. Ding, B. Ziebarth, M.J. Davis, J.C. Mauro, J. Am. Ceram. Soc. 103, 4295 (2020).
77. S. Kapoor, R.E. Youngman, L. Ma, N. Lönnroth, S.J. Rzoska, M. Bockowski, L.R. Jensen, M. Bauchy, M.M. Smedskjaer, Front. Mater. 6, 1 (2019).

78. S. Kapoor, N. Lönnroth, R.E. Youngman, S.J. Rzoska, M. Bockowski, L.R. Jensen, M.M. Smedskjaer, J. Non-Cryst. Solids 469, 31 (2017).
79. S. Kapoor, X. Guo, R.E. Youngman, C.L. Hogue, J.C. Mauro, S.J. Rzoska, M. Bockowski, L.R. Jensen, M.M. Smedskjaer, Phys. Rev. Appl. 7, 054011 (2017).
80. S. Kapoor, K. Januchta, R.E. Youngman, X. Guo, J.C. Mauro, M. Bauchy, S.J. Rzoska, M. Bockowski, L.R. Jensen, M.M. Smedskjaer, Phys. Rev. Mater. 2, 063603 (2018).
81. Y. Shu, Y. Kono, I. Ohira, Q. Li, R. Hrubiak, C. Park, C. Kenney-Benson, Y. Wang, G. Shen, J. Phys. Chem. Lett. 11, 374 (2020).
82. M. Durandurdu, J. Am. Ceram. Soc. 100, 3903 (2017).
83. L. P. Davila, M.-J. Caturla, A. Kubota, B. Sadigh, T. D. de la Rubia, J. F. Shackelford, S. H. Risbud, S. H. Garofalini, Phys. Rev. Lett. 91, 205501 (2003).
84. T. Rouxel, H. Ji, T. Hammouda, A. Moréac, Phys. Rev. Lett. 100, 225501 (2008).
85. M. M. Smedskjaer, R. E. Youngman, S. Striepe, M. Potuzak, U. Bauer, J. Deubener, H. Behrens, J. C. Mauro, Y. Yue, Sci. Rep. 4, 3770 (2014).
86. T. Rouxel, J. Am. Ceram. Soc. 90, 3019 (2007).
87. K. G. Aakermann, K. Januchta, J. A. Pedersen, M. N. Svenson, S. J. Rzoska, M. Bockowski, J. C. Mauro, M. Guerette, L. Huang, M. M. Smedskjaer, J. Non Cryst. Solids 426, 175 (2015).
88. M. N. Svenson, M. Guerette, L. Huang, N. Lönnroth, J. C. Mauro, S. J. Rzoska, M. Bockowski, M. M. Smedskjaer, Chem. Phys. Lett. 651, 88 (2016).
89. K. Januchta, R. Sun, L. Huang, M. Bockowski, S. J. Rzoska, L. R. Jensen, M. M. Smedskjaer, J. Non-Cryst. Solids 494, 86 (2018).
90. T. K. Bechgaard, A. Goel, R. E. Youngman, J. C. Mauro, S. J. Rzoska, M. Bockowski, L. R. Jensen, M. M. Smedskjaer, J. Non Cryst. Solids 441, 49 (2016).
91. S. Striepe, M. M. Smedskjaer, J. Deubener, U. Bauer, H. Behrens, M. Potuzak, R. E. Youngman, J. C. Mauro, Y. Yue, J. Non-Cryst. Solids 364, 44 (2013).
92. K. Januchta, R. E. Youngman, A. Goel, M. Bauchy, S. J. Rzoska, M. Bockowski, M. M. Smedskjaer, J. Non-Cryst. Solids 460, 54 (2017).

93. K.-H. Lee, Y. Yang, L. Ding, B. Ziebarth, J. C. Mauro, J. Am. Ceram. Soc. 105, 2536 (2022).

94. M. Ono, S. Aoyama, M. Fujinami, S. Ito, Opt. Express 26, 7942 (2018).

95. Y. Yang, O. Homma, S. Urata, M. Ono, J. C. Mauro, npj Comput. Mater. 6, 139 (2020).

96. A. Cornet, C. Martinet, V. Martinez, D. De Ligny, J. Chem. Phys. 151, 164502 (2019).

97. A. Cornet, V. Martinez, D. De Ligny, B. Champagnon, C. Martinet, J. Chem. Phys. 146, 094504 (2017).

98. O.B. Tsiok, V. V. Brazhkin, A.G. Lyapin, L.G. Khvostantsev, Phys. Rev. Lett. 80, 999 (1998).

99. O. Mishima, L.D. Calvert, E. Whalley, Nature 314, 76 (1985).

100. Y. Onodera, S. Kohara, S. Tahara, A. Masuno, H. Inoue, M. Shiga, A. Hirata, K. Tsuchiya, Y. Hiraoka, I. Obayashi, K. Ohara, A. Mizuno, O. Sakata, J. Ceram. Soc. Japan 127, 853 (2019).

101. Q. Zhou, Y. Shi, B. Deng, J. Neuefeind, M. Bauchy, Sci. Adv. 7, eabh1761 (2021).

102. A. Zeidler, K. Wezka, D.A.J. Whittaker, P.S. Salmon, A. Baroni, S. Klotz, H.E. Fischer, M.C. Wilding, C.L. Bull, M.G. Tucker, M. Salanne, G. Ferlat, M. Micoulaut, Phys. Rev. B 90, 024206 (2014).

103. B. Hehlen, J. Phys.: Condens. Matter 22, 025401 (2010).

104. L. Giacomazzi, P. Umari, A. Pasquarello, Phys. Rev. B 79, 064202 (2009).

105. M. Ropo, J. Akola, R.O. Jones, Phys. Rev. B 96, 184102 (2017).

106. Y. Onodera, S. Kohara, P.S. Salmon, A. Hirata, N. Nishiyama, S. Kitani, A. Zeidler, M. Shiga, A. Masuno, H. Inoue, S. Tahara, A. Polidori, H.E. Fischer, T. Mori, S. Kojima, H. Kawaji, A.I. Kolesnikov, M.B. Stone, M.G. Tucker, M.T. McDonnell, A.C. Hannon, Y. Hiraoka, I. Obayashi, T. Nakamura, J. Akola, Y. Fujii, K. Ohara, T. Taniguchi, O. Sakata, NPG Asia Mater 12, 85 (2020).

107. M. Ono, K. Hara, M. Fujinami, S. Ito, Appl. Phys. Lett. 101, 164103 (2012).

108. I. Heimbach, F. Rhiem, F. Beule, D. Knodt, J. Heinen, R.O. Jones, J. Comput. Chem. 38, 389 (2017).

109. T.F. Willems, C.H. Rycroft, M. Kazi, J.C. Meza, M. Haranczyk, Microporous Mesoporous Mater. 149, 134 (2012).

110. H. Tanaka, H. Tong, R. Shi, J. Russo, Nat. Rev. Phys. 1, 333 (2019).

111. S.S. Sørensen, C.A.N. Biscio, M. Bauchy, L. Fajstrup, M.M. Smedskjaer, Sci. Adv. 6, eabc2320 (2020).

112. Y. Hiraoka, T. Nakamura, A. Hirata, E.G. Escolar, K. Matsue, Y. Nishiura, Proc. Natl. Acad. Sci. U.S.A. 113, 7035 (2016).

113. Y. Onodera, Y. Takimoto, H. Hijiya, T. Taniguchi, S. Urata, S. Inaba, S. Fujita, I. Obayashi, Y. Hiraoka, S. Kohara, NPG Asia Mater 11, 75 (2019).

114. T. Nakamura, Y. Hiraoka, A. Hirata, E.G. Escolar, Y. Nishiura, Nanotechnol. 26, 304001 (2015).

115. L. Pauling, J. Am. Chem. Soc. 51, 1010 (1929).

116. A. Pandey, P. Biswas, D.A. Drabold, Phys. Rev. B 92, 155205 (2015).

117. Y. Yang, J. Zhou, F. Zhu, D. Chang, D.S. Kim, Y. Yuan, M. Pham, A. Rana, X. Tian, Y. Yao, S. Osher, L. Hu, P. Ercius, J. Miao, Nature 592, 60 (2021).

118. T. Du, H. Liu, L. Tang, S.S. Sørensen, M. Bauchy, M.M. Smedskjaer, ACS Nano 15, 17705 (2021).

119. Y. Shang, Z. Liu, J. Dong, M. Yao, Z. Yang, Q. Li, C. Zhai, F. Shen, X. Hou, L. Wang, N. Zhang, W. Zhang, R. Fu, J. Ji, X. Zhang, H. Lin, Y. Fei, B. Sundqvist, W. Wang, B. Liu, Nature 599, 599 (2021).

AIP Publishing

Journal of Applied Physics

ACCEPTED MANUSCRIPT

PLEASE CITE THIS ARTICLE AS DOI: 10.1063/5.0088606

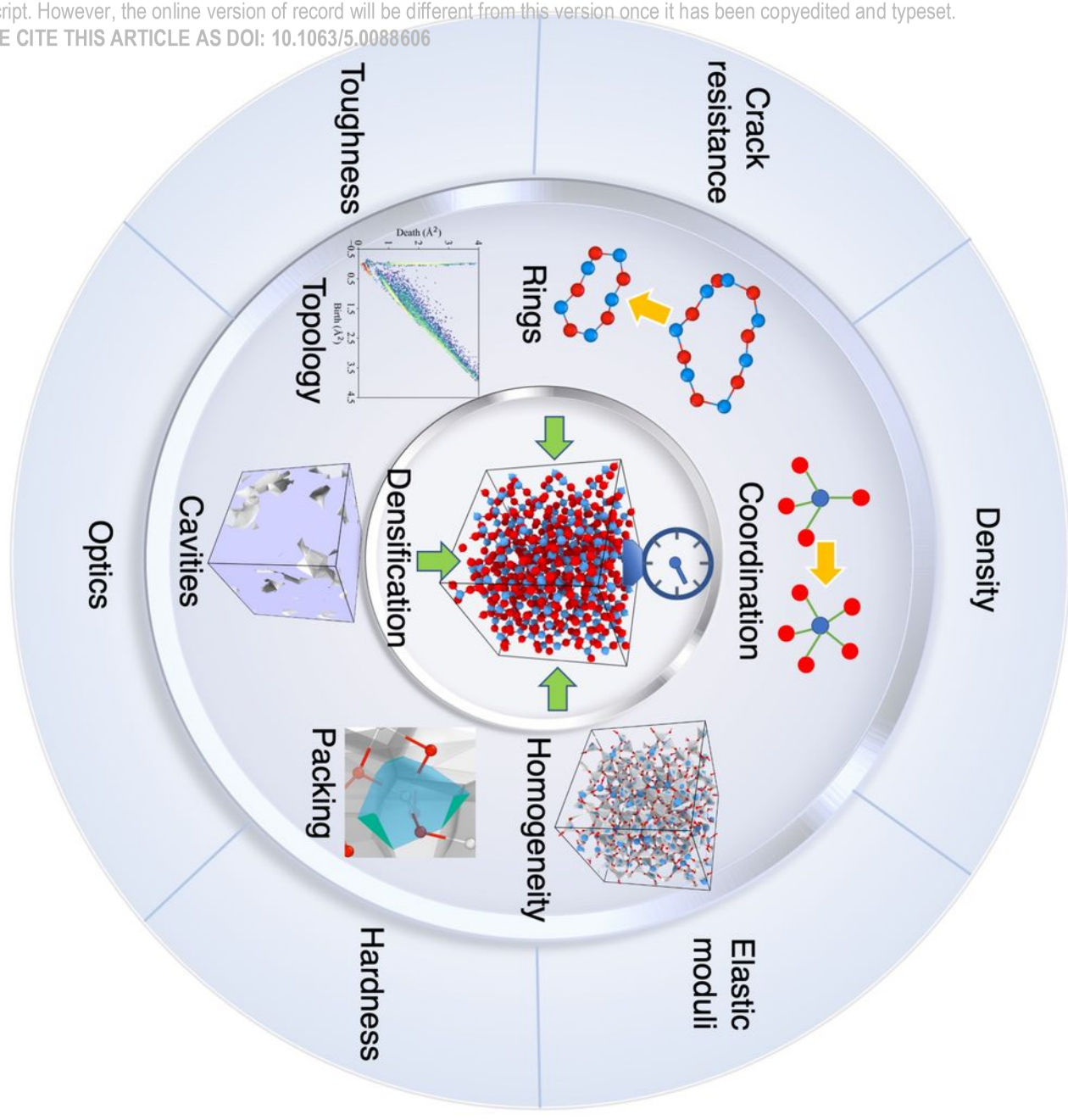

Journal of Applied Physics

AIP Publishing

(a)

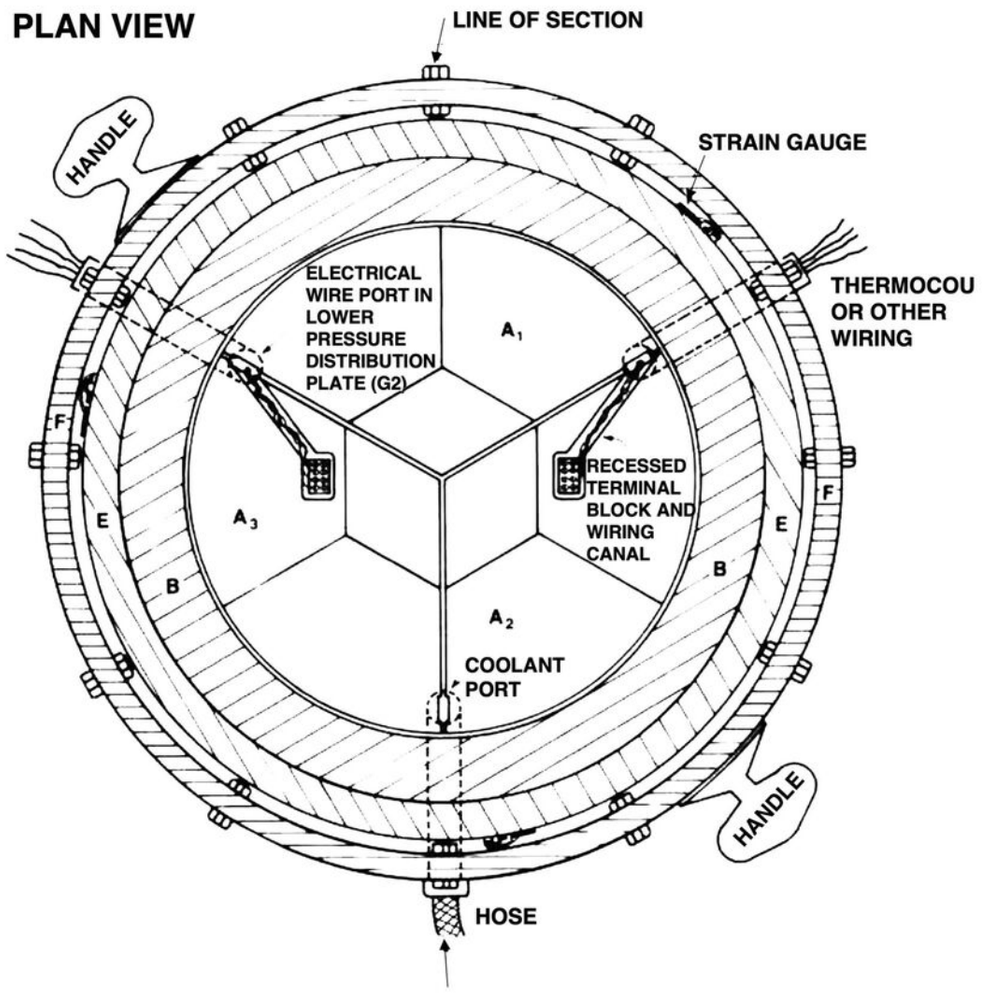

(b)

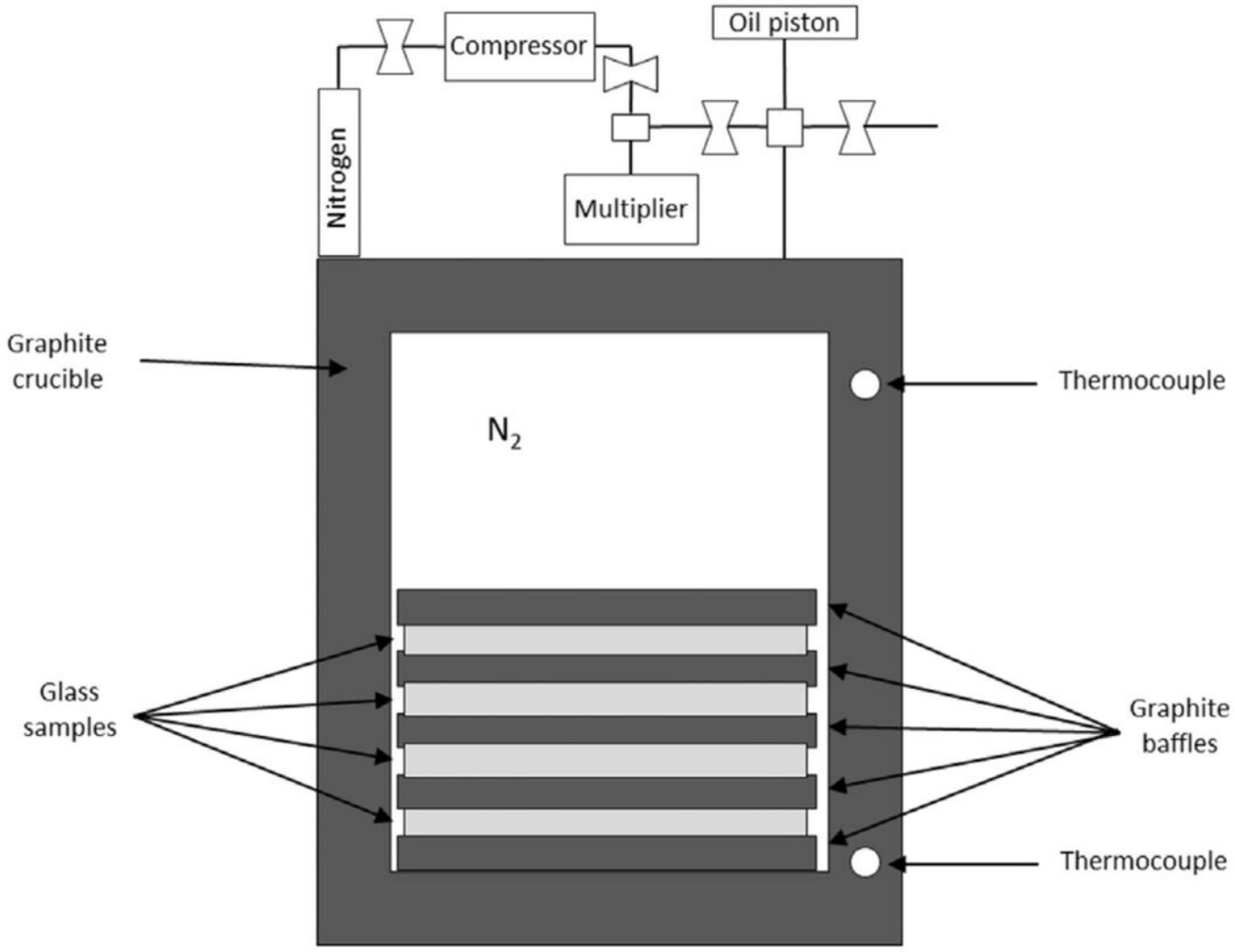

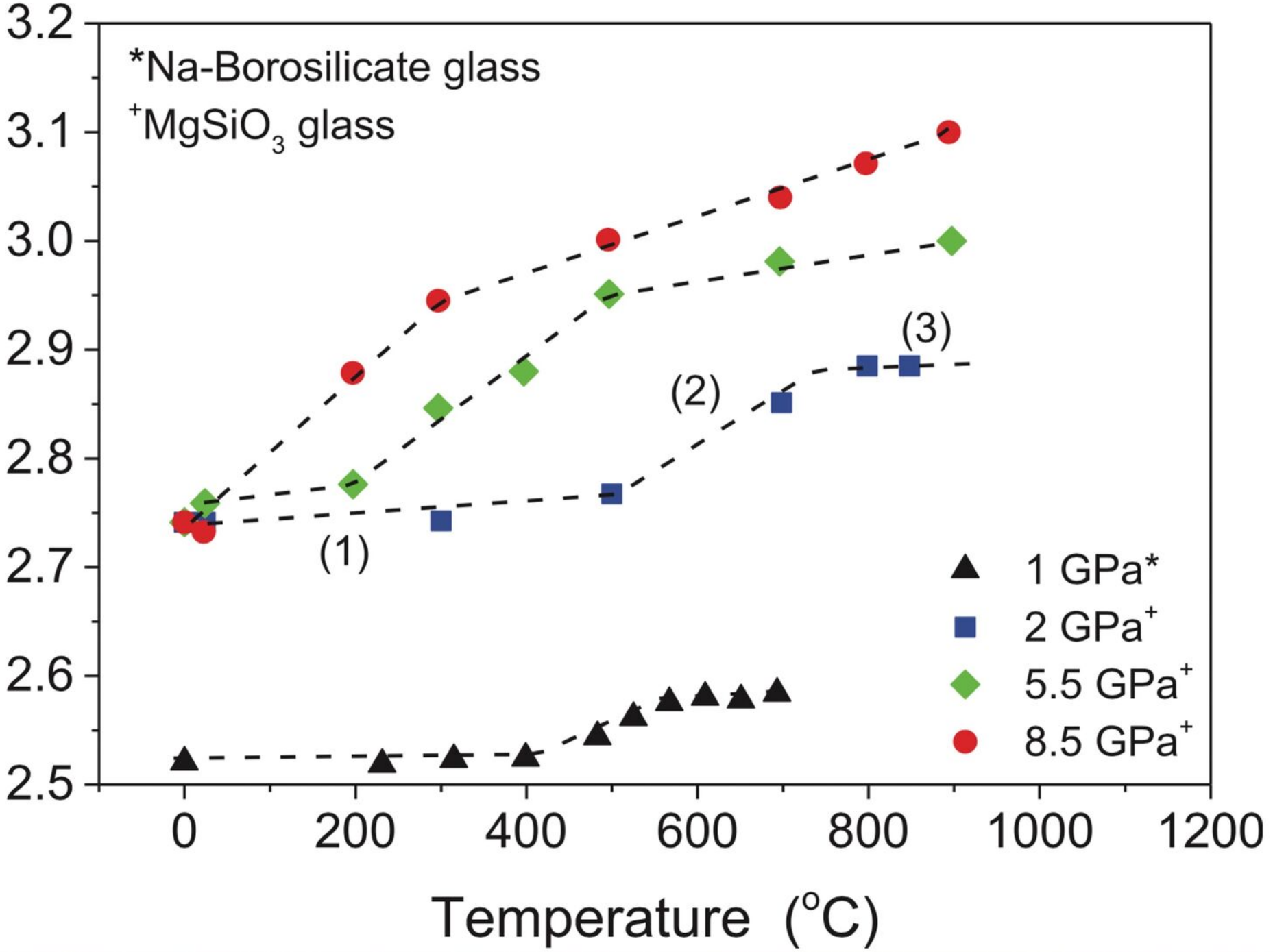

Journal of Applied Physics

AIP Publishing

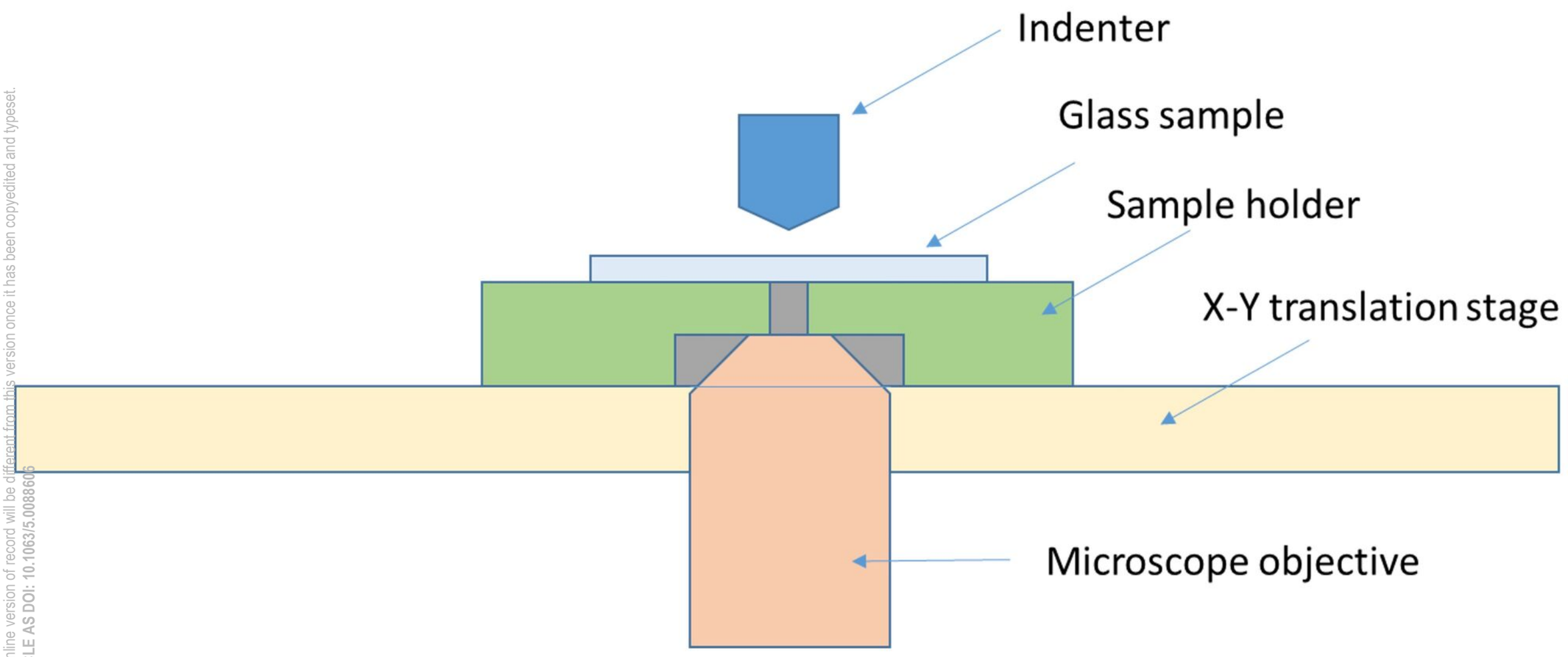

AIP Publishing
Journal of Applied Physics
ACCEPTED MANUSCRIPT

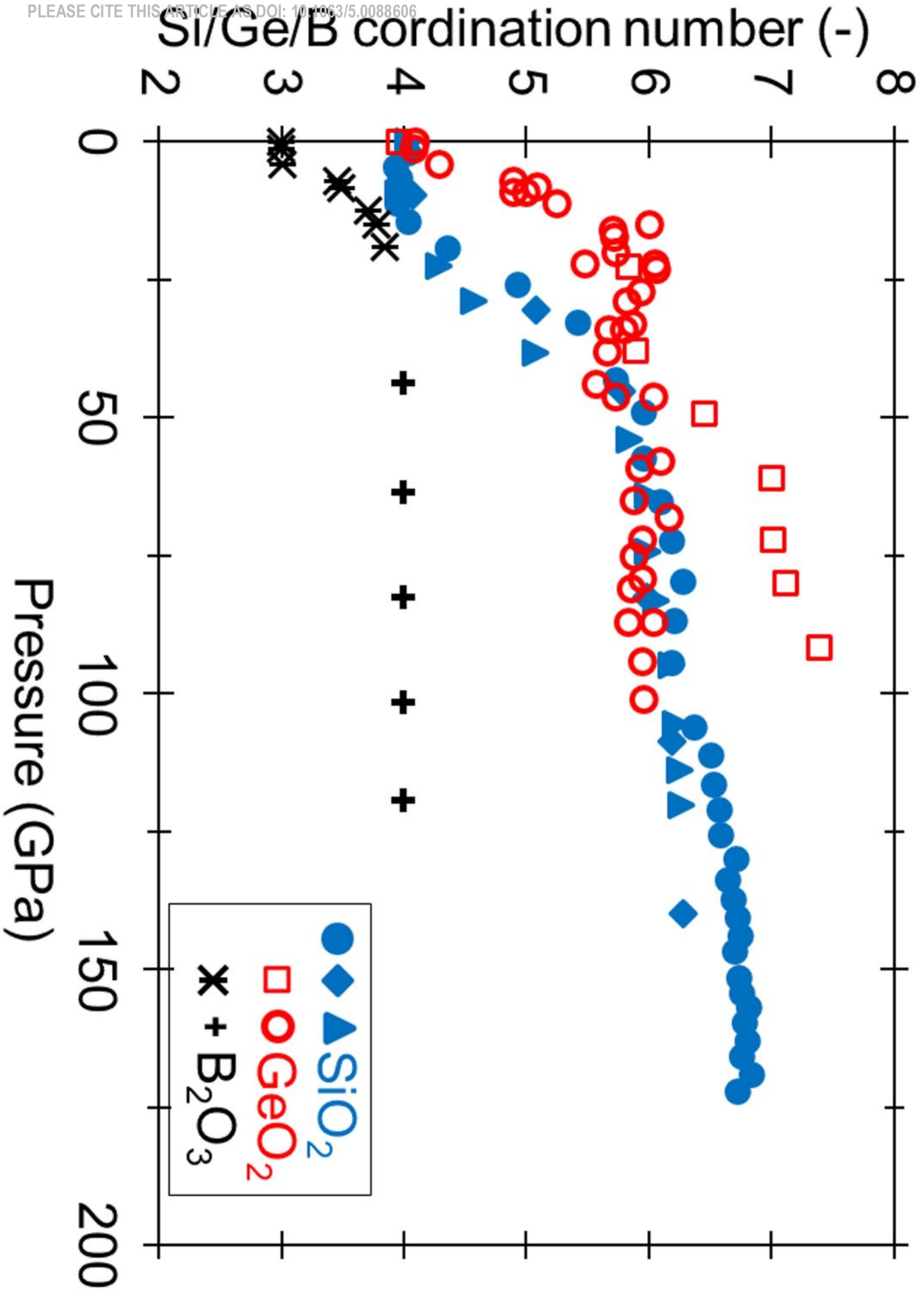

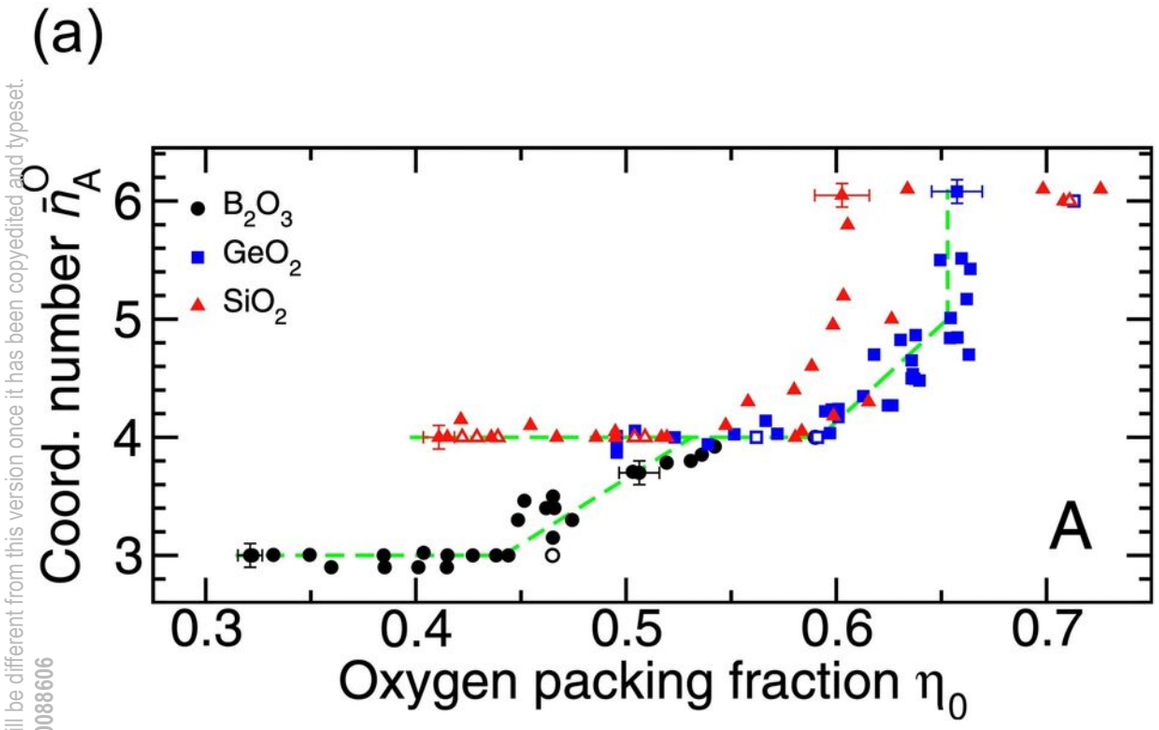

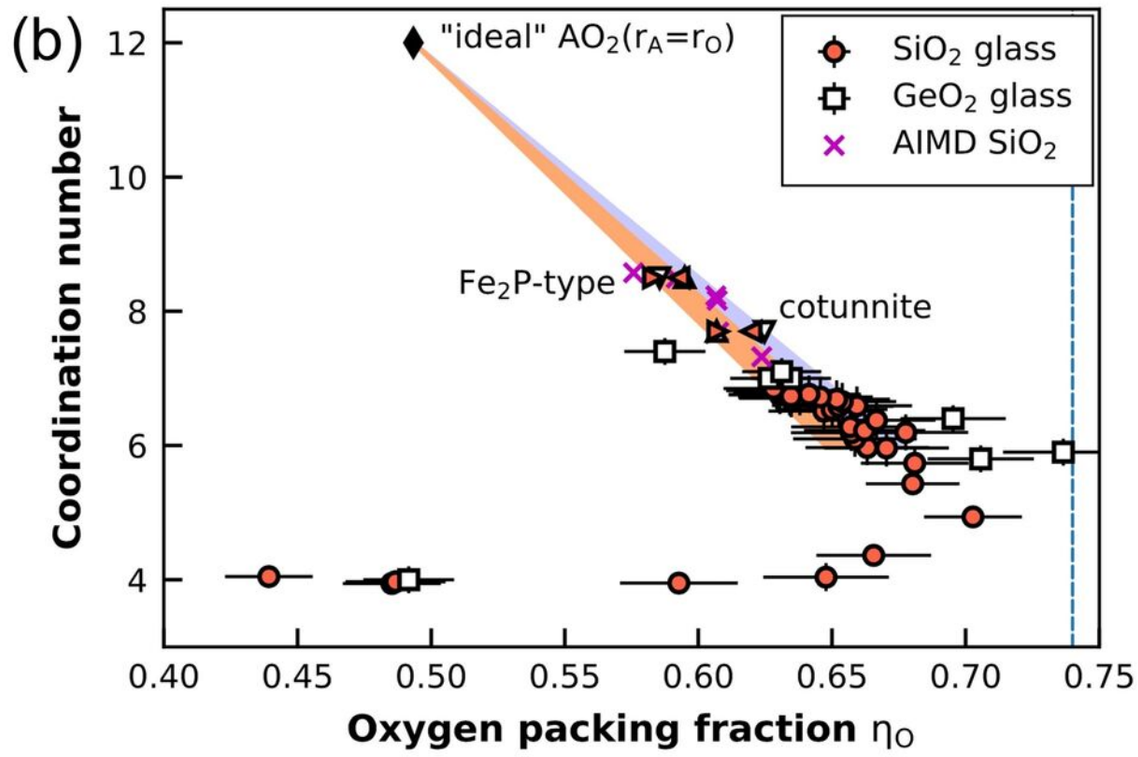

Journal of Applied Physics

AIP Publishing

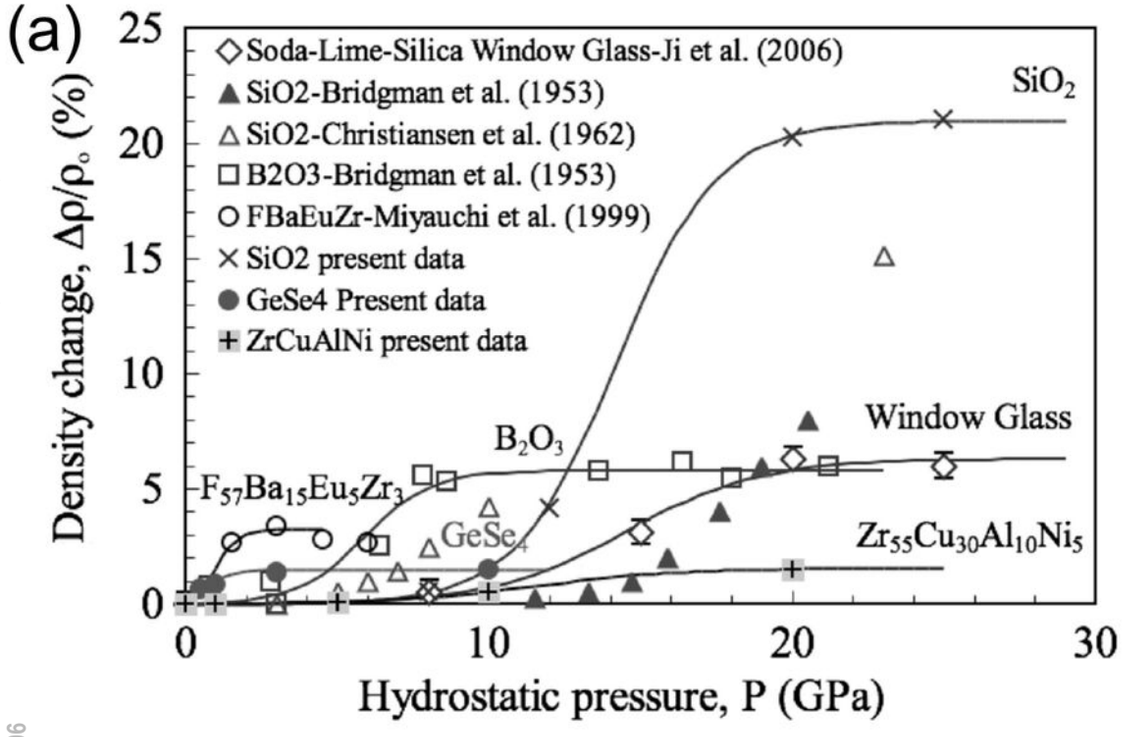

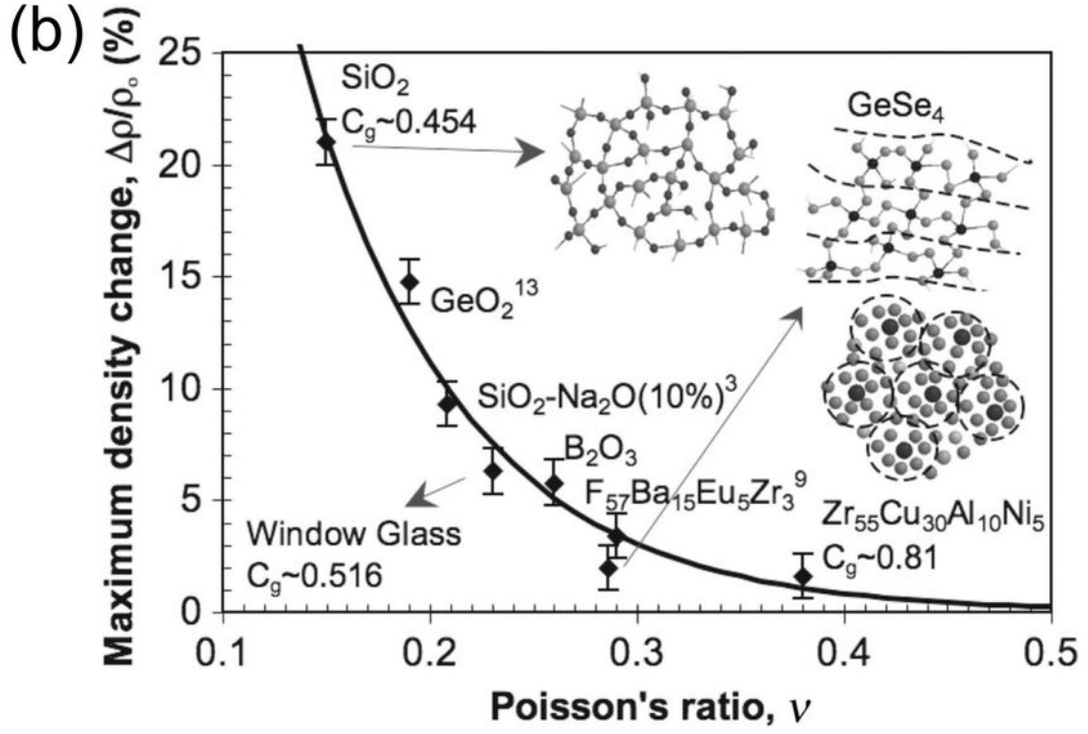

Journal of Applied Physics

PLEASE CITE THIS ARTICLE AS DOI: 10.1063/5.0088606

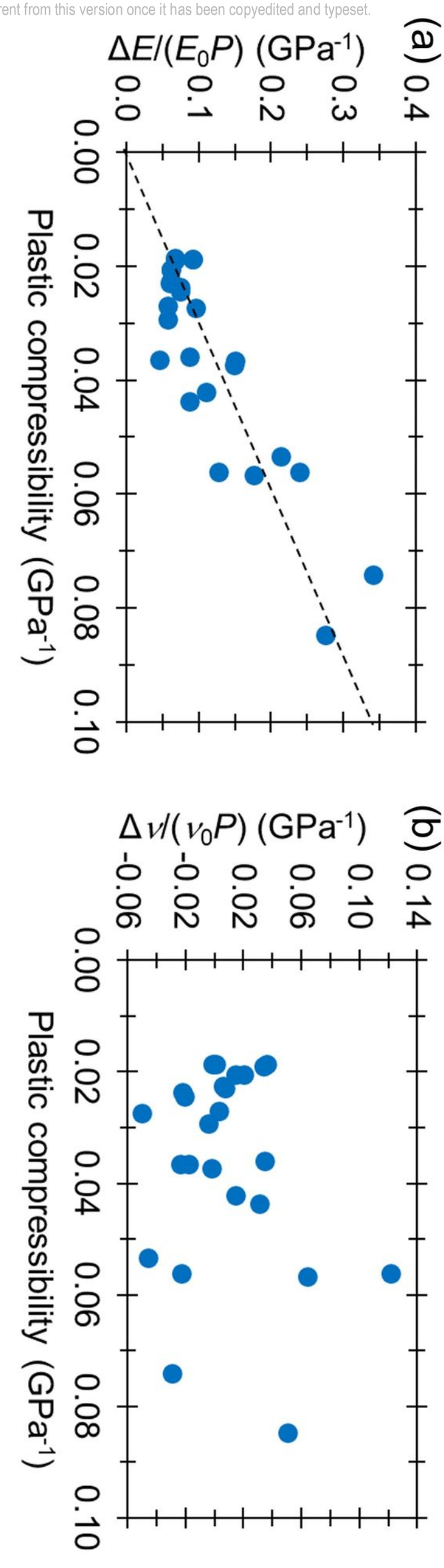

Journal of Applied Physics

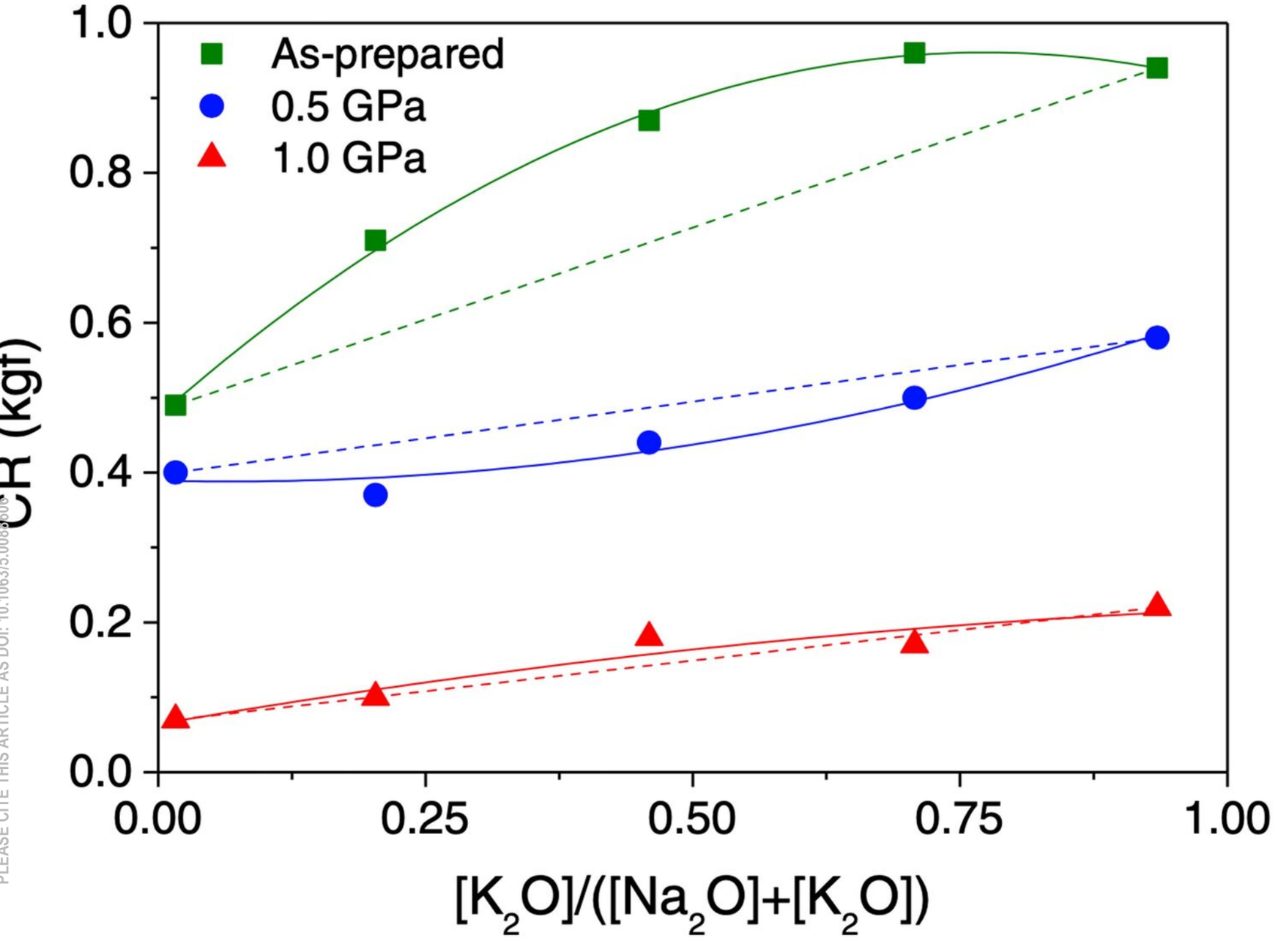

AIP Publishing

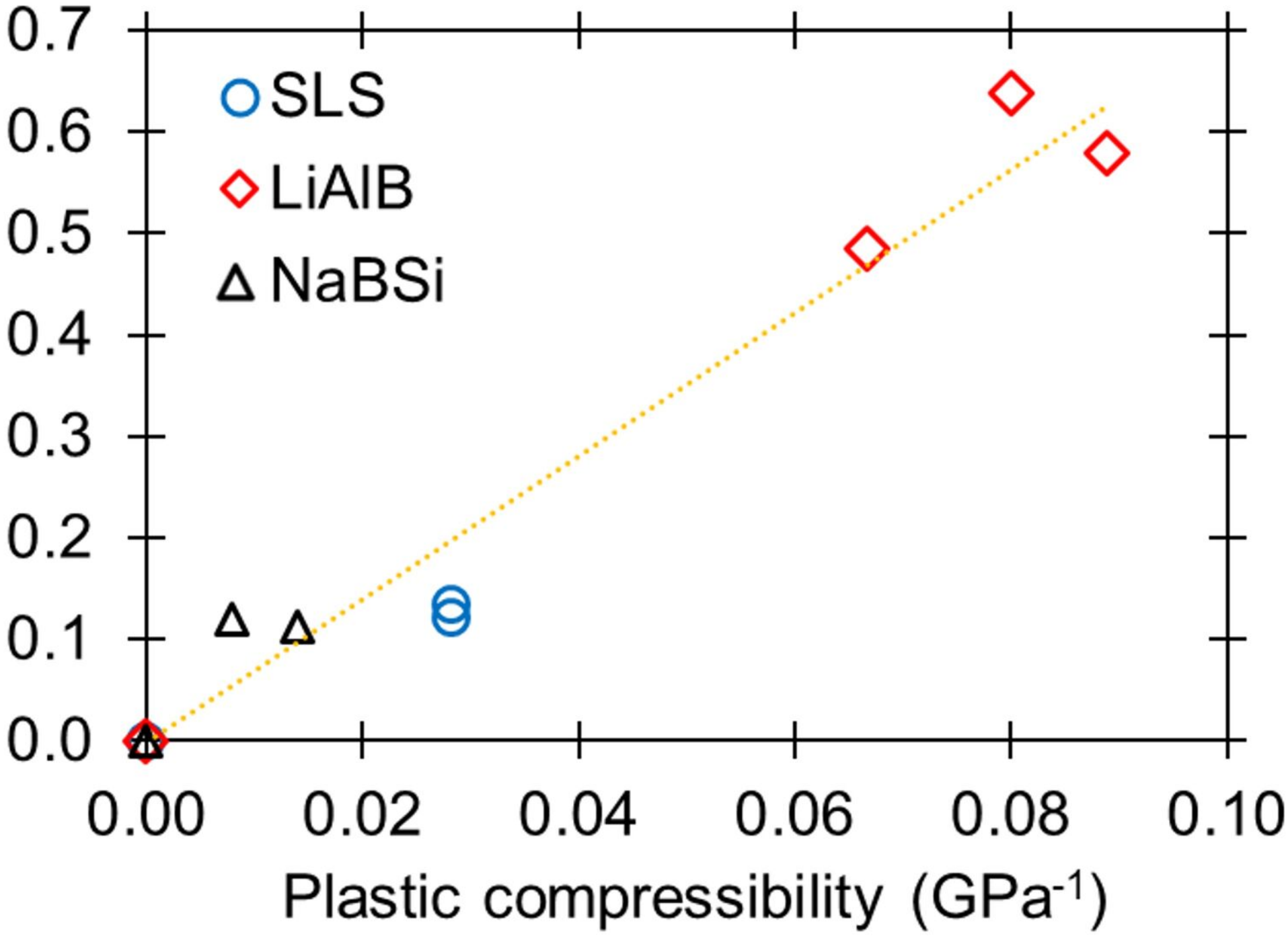

AIP Publishing

Journal of Applied Physics

ACCEPTED MANUSCRIPT

This is the author's peer reviewed, accepted manuscript. However, the online version of record will be different from this version once it has been copyedited and typeset.
PLEASE CITE THIS ARTICLE AS DOI: 10.1063/5.0088606

Journal of Applied Physics

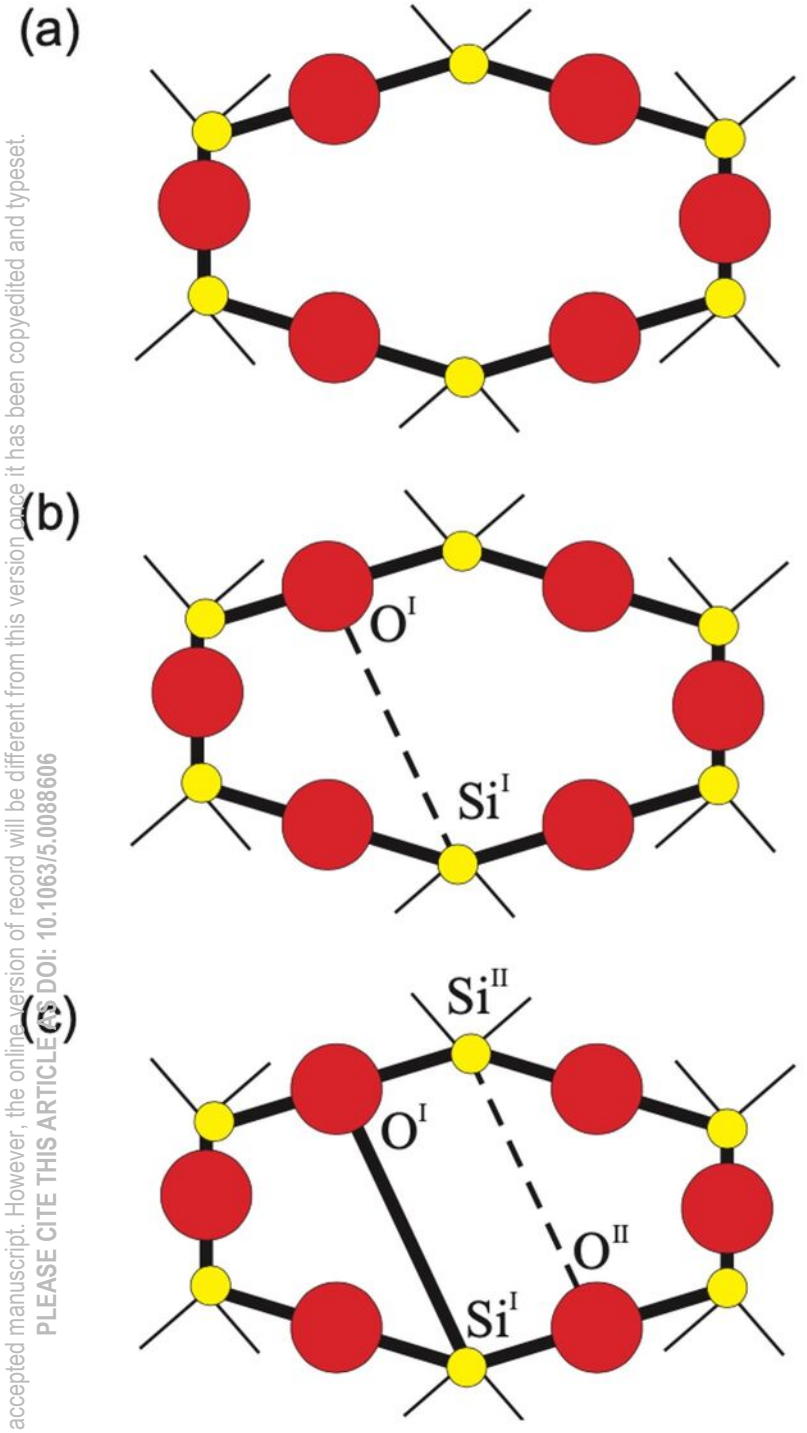

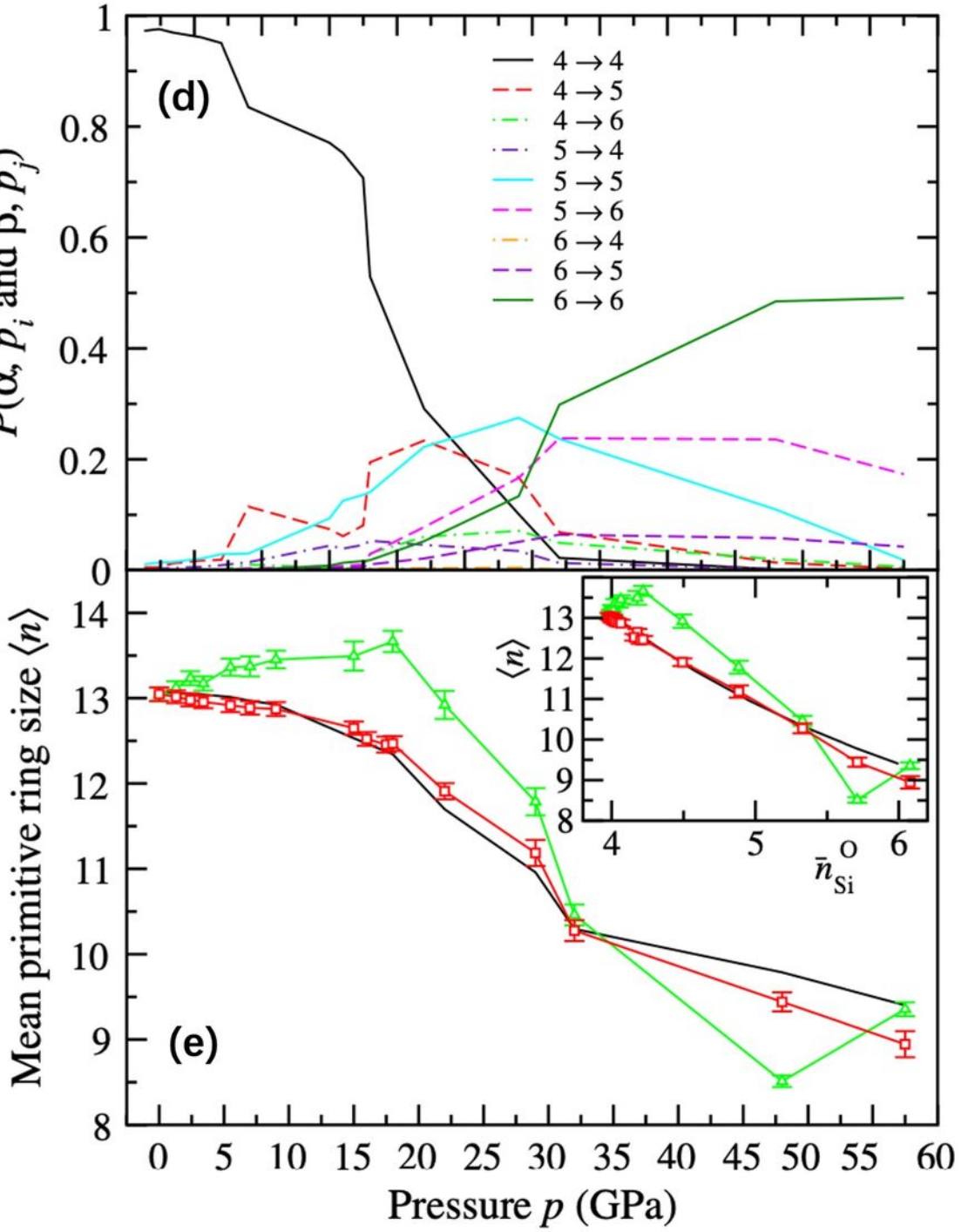

Journal of Applied Physics

AIP Publishing

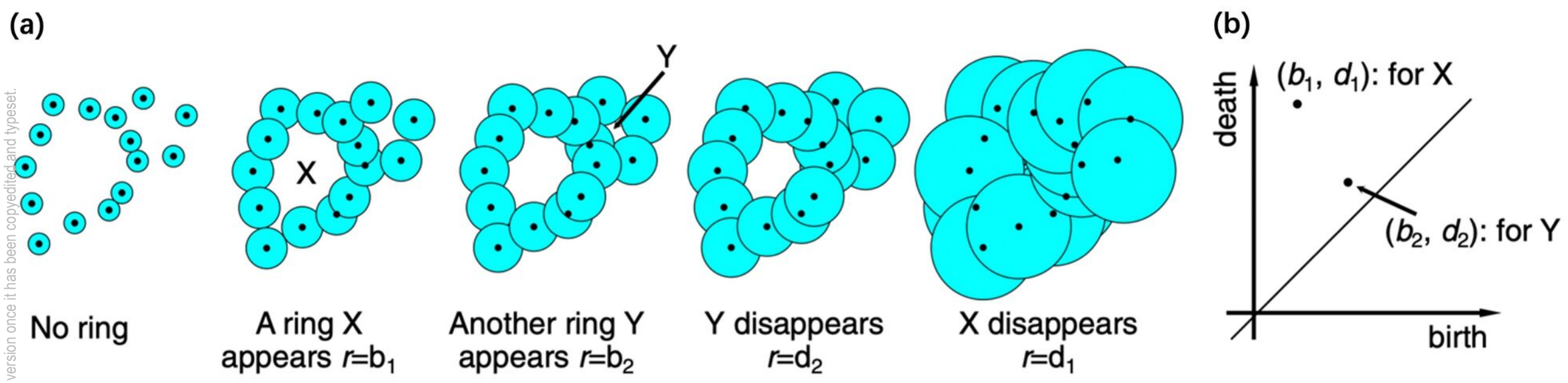

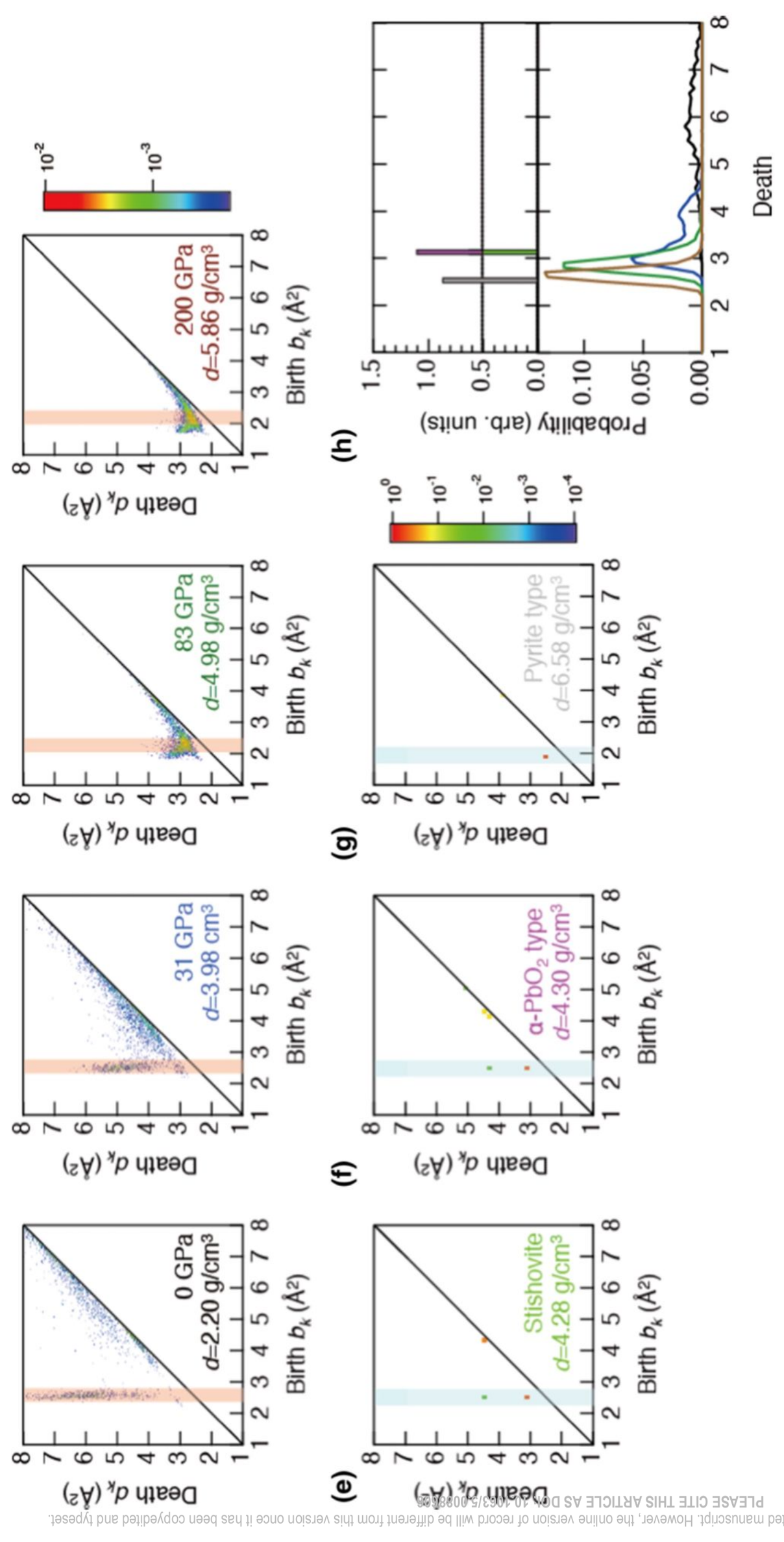

Journal of Applied Physics

AIP Publishing

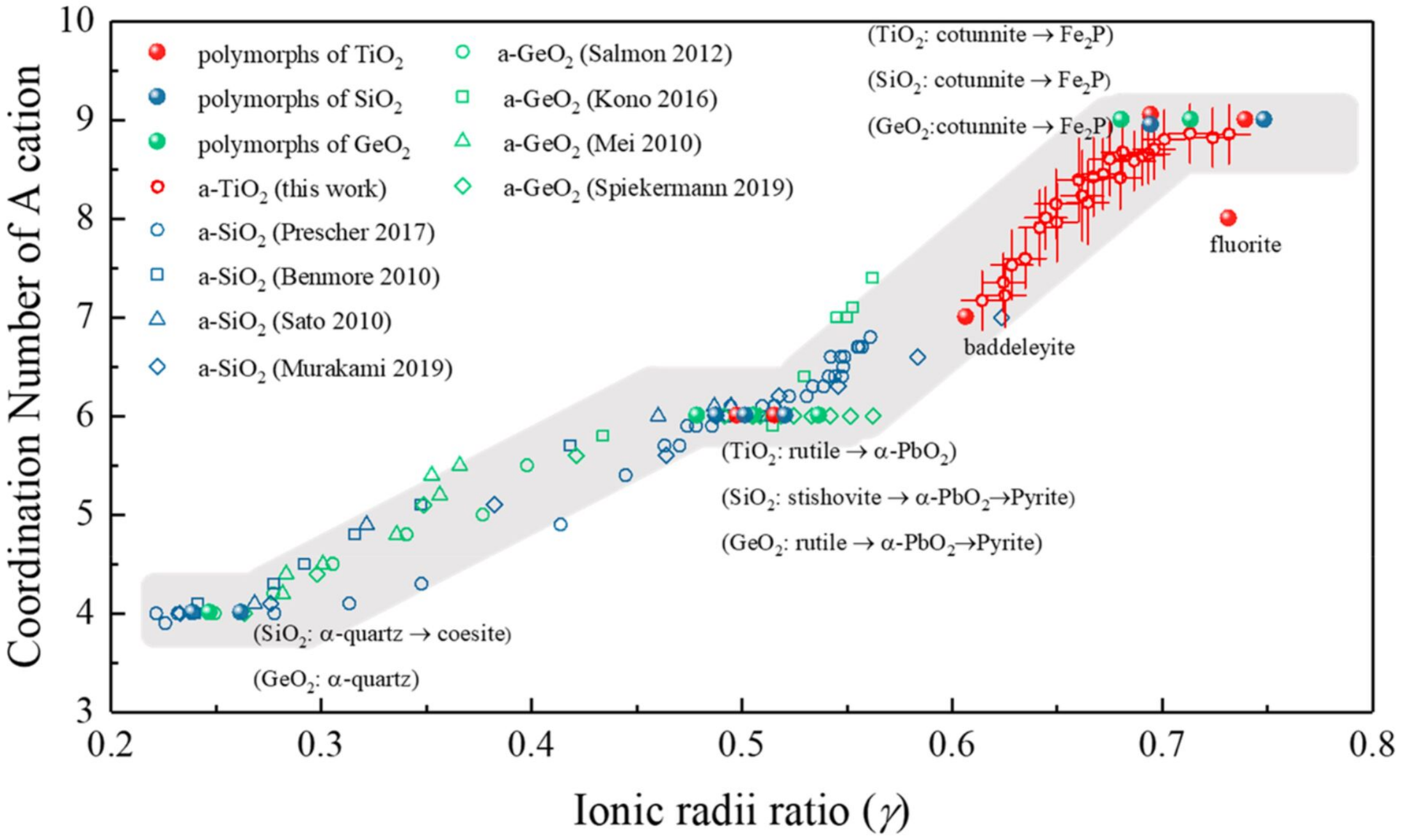

AIP Publishing

Journal of Applied Physics

ACCEPTED MANUSCRIPT

PLEASE CITE THIS ARTICLE AS DOI: 10.1063/5.0088606